# 1 Basic Physics of Intersubband Radiative and Nonradiative Processes

Jacob B. Khurgin

Johns Hopkins University

Intersubband (ISB) transitions were first observed experimentally in the 1980s [1] and immediately attracted attention due to their unique properties, of which the ability to be designed for a specific wavelength in the infrared (IR) range of the spectrum is perhaps the most significant one. Soon thereafter IR detectors based on the ISB transitions – quantum well intersubband detectors [2, 3] as well as incoherent emitters [4] – were realized, and in the following decade the Intersubband lasers, QCLs [5–7], which are the subject of this book, were developed. In addition to the flexibility of design, ISB transitions have a large oscillator strength, which allows one to create efficient sources and detectors that are only a few micrometers (i.e., a fraction of wavelength) thick. The concept of intersubband transition is easily understood using a simple potential-well model from any physics textbook, but this model does not provide an explanation of how the ISB transition is related to the interband transitions and how their strengths compare [8]. In this chapter we shall establish this connection, explain the selection rules, and point out that for the same frequency the interband and ISB transitions are just about equally strong, which explains why the interband cascade lasers (ICLs) that have been in development since the late 1990s [9, 10] provide strong competition to QCLs in the shorter wavelength range of the IR spectrum. The physics of ISB transitions [6, 11] is the subject of the first two sections of this chapter.

In Section 1.3 we describe the nonradiative ISB transitions which play an important role in the operation of QCLs. Specifically, we explain how the strong interaction between electrons and polar longitudinal-optical phonons, leading to picosecond-scale transitions within and between subbands, enables population inversion and lasing. We also discuss other important processes such as electron-electron scattering that thermalizes electrons within a given subband, interface-roughness (IFR) scattering that causes both transition broadening and transition-lifetime shortening, and alloy-disorder (AD) scattering, which also causes transition-lifetime shortening (this fact, for both IFR and AD scattering, being often underappreciated). The short background provided by this chapter is by no means a substitute for in-depth knowledge of the physics of semiconductor quantum wells and superlattices, which can be gained from a number of excellent texts on this subject [11–14]. Nevertheless, it aims to provide background sufficient for understanding the operation of various QCL designs that are covered in the rest of this book.
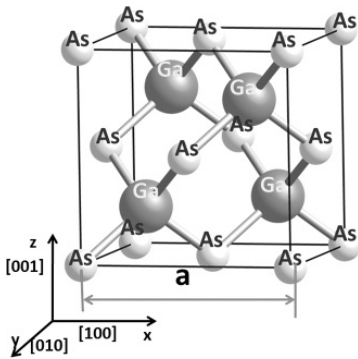
**Fig. 1.1** Zinc-blende crystal lattice of a typical III-V semiconductor (GaAs).

## 1.1 Electronic States in the III-V Semiconductor Quantum Wells

### 1.1.1 The Basis States and the Bond Orbital Picture

Although there have been attempts to generate infrared radiation using intersubband transitions in a wide range of semiconductors, at this time all practical QCLs are based on covalent III-V semiconductors, consisting of a group III (Al, In, or Ga) cations and group V (P, As, or Sb) anions arranged in a zinc-blende (ZB) cubic lattice. If only one species of anion and cation constitute the material, then it is called a binary alloy, such as, for instance, GaAs and InP. Otherwise, materials can be ternary (e.g., $Al_xGa_{1-x}As$ or $InAs_xP_{1-x}$) or quaternary (e.g., $In_y Ga_{1-y}As_xP_{1-x}$) alloys. The composition of ternary- and quaternary-alloy materials is usually designed in such a way that their lattice constant is identical (or close) to that of a binary-alloy substrate, usually InP or GaAs, although alternative substrates have also been considered. It is the ability to adjust the composition of quantum wells (QWs) and their geometry that allows one to design the structures with ISB transitions over a wide range of IR and THz frequencies.

In the ZB lattice (Fig. 1.1) each group III cation atom is surrounded by four group V anion atoms in a tetragonal configuration and vice versa each group V ion is surrounded by four group III ions, thus, there are four tetragonal bonds directed along four diagonals of the cube – the $<111>$ crystallographic directions. The bonds are formed by hybridization. Hybridization is a process by which first the four valence orbitals of each ion – one S-type $\left|S_{a,c}\right\rangle$ and three P-type: $\left|X_{a,c}\right\rangle$, $\left|Y_{a,c}\right\rangle$, $\left|Z_{a,c}\right\rangle$, all shown in Fig. 1.2, form four hybrid orbitals (Fig. 1.3) [15, 16],

$$
\begin{aligned}
\left|H_{a,c}^{(1)}\right\rangle &= \frac{1}{2}\left|S_{a,c}\right\rangle + \frac{1}{2}\left|X_{a,c}\right\rangle + \frac{1}{2}\left|Y_{a,c}\right\rangle + \frac{1}{2}\left|Z_{a,c}\right\rangle, \\
\left|H_{a,c}^{(2)}\right\rangle &= \frac{1}{2}\left|S_{a,c}\right\rangle + \frac{1}{2}\left|X_{a,c}\right\rangle - \frac{1}{2}\left|Y_{a,c}\right\rangle - \frac{1}{2}\left|Z_{a,c}\right\rangle, \\
\left|H_{a,c}^{(3)}\right\rangle &= \frac{1}{2}\left|S_{a,c}\right\rangle - \frac{1}{2}\left|X_{a,c}\right\rangle - \frac{1}{2}\left|Y_{a,c}\right\rangle + \frac{1}{2}\left|Z_{a,c}\right\rangle, \\
\left|H_{a,c}^{(4)}\right\rangle &= \frac{1}{2}\left|S_{a,c}\right\rangle - \frac{1}{2}\left|X_{a,c}\right\rangle + \frac{1}{2}\left|Y_{a,c}\right\rangle - \frac{1}{2}\left|Z_{a,c}\right\rangle,
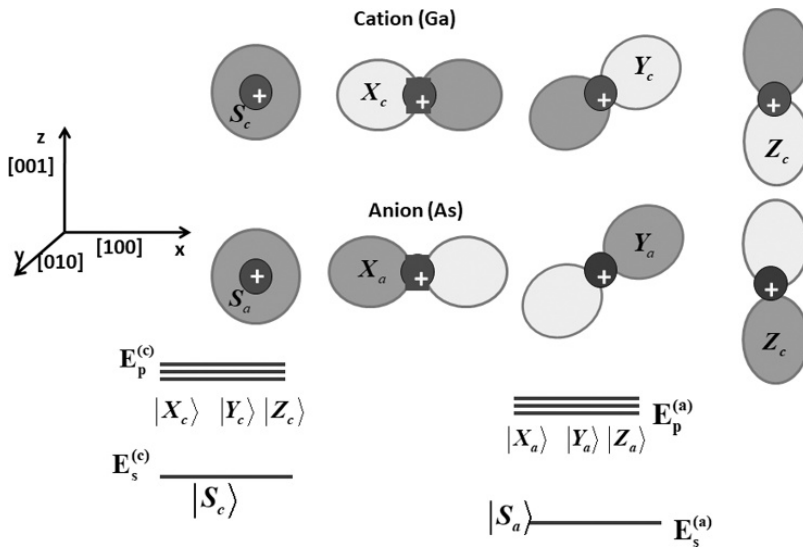\end{aligned}
\tag{1.1}
$$

**Fig. 1.2** Basis states of four valence orbitals for cation and anion and their energies.

where indices a and c indicate anion and cation, respectively, from the four hybrid orbitals, and then each pair of hybrid orbitals directed towards each other form bonding,

$$\left| H_+^{(i)} \right\rangle = \alpha \left| H_a^{(i)} \right\rangle + \beta \left| H_c^{(i)} \right\rangle, \tag{1.2}$$

and anti-bonding,

$$\left| H_-^{(i)} \right\rangle = \beta \left| H_a^{(i)} \right\rangle - \alpha \left| H_c^{(i)} \right\rangle, \tag{1.3}$$

orbitals separated by the energy gap (which is **not** the fundamental direct energy gap related to the absorption edge). Four bonding orbitals are all filled with eight valence electrons shared by each anion–cation pair and thus constitute a fully occupied valence band. Four unfilled anti-bonding orbitals form the empty conduction band, and the energy difference between two bands represents the binding energy holding the crystal together. Since the bond is polar $\alpha > 1/\sqrt{2} > \beta$ indicating that electrons in the conduction band tend to be located near the group V anion (which is therefore negatively charged) and the electrons in the conduction band are to be found closer to the group III cation.

The above "bond orbitals" picture adequately describes the general features of ZB covalent semiconductors: the presence of a bandgap, mechanical hardness (due to the rigid "skeleton" formed by bonds), a relatively large dielectric constant (the latter due to long polarizable bonds), piezoelectricity, and optical nonlinearity (due to lack of central symmetry), as well as other properties. However, in order to understand the most relevant QCL electrical and optical properties one must consider the band structure near the center of the Brillouin zone, i.e., the states

$$u_{c,v}(\boldsymbol{k})e^{i\boldsymbol{k}\cdot\boldsymbol{r}}, \tag{1.4}$$
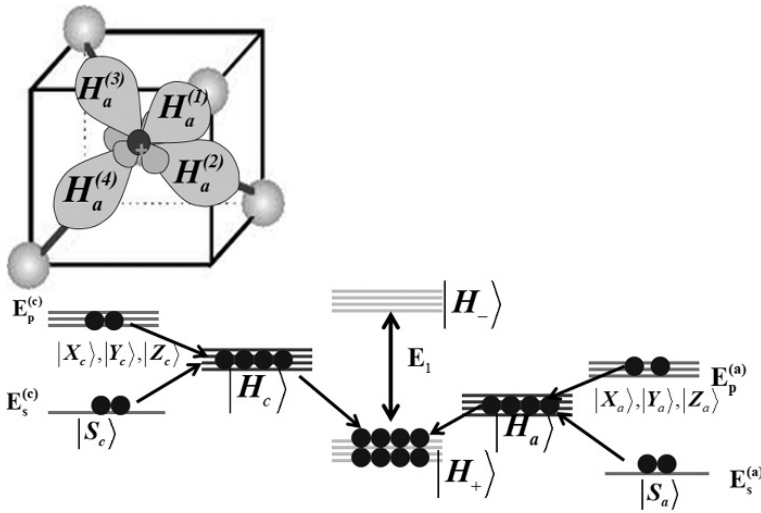
**Fig. 1.3** Four hybrid orbitals that bind the zinc-blende lattice and the energy diagram of hybrid bonding and anti-bonding schemes.

where $\mathbf{k}$ is the wavevector and $u_{c,v}(\mathbf{k})$ is the periodic wave Bloch function. At the center of BZ, where $\mathbf{k} = 0$, the conduction and valence states split into triple-degenerate bonding and anti-bonding P-type states, and nondegenerate bonding and anti-bonding S-type states as shown in Fig. 1.4.

We thus obtain (see Fig. 1.5) the following states:

- The lowest valence-band (VB) state with energy $E_{s+} \sim -10$ eV,

$$u_{v1}(0) = \left|S_+\right\rangle = \alpha\left|S_a\right\rangle + \beta\left|S_c\right\rangle, \tag{1.5}$$

which is a bonding combination of S-like orbitals of cations and anions. This band plays virtually no role in the interactions relevant to QCL operation and will from now on be neglected.

- Three degenerate valence band states with energy $E_{p+}$, which we take to be equal to zero:

$$u_{v2}(0) = \left|X_+\right\rangle = \alpha\left|X_a\right\rangle + \beta\left|X_c\right\rangle,$$
$$u_{v3}(0) = \left|Y_+\right\rangle = \alpha\left|Y_a\right\rangle + \beta\left|Y_c\right\rangle, \tag{1.6}$$
$$u_{v4}(0) = \left|Z_+\right\rangle = \alpha\left|Z_a\right\rangle + \beta\left|Z_c\right\rangle.$$

These are the bonding combinations of P-like orbitals. These states are the ones in which the holes reside and are also the ones that mix with conduction-band (CB) states in QWs and are therefore extremely important for ISVB transitions.

- The lowest CB state with energy $E_{s-} = E_g$,

$$u_{c1}(0) = \left|iS_-\right\rangle = i\beta\left|S_a\right\rangle - i\alpha\left|S_c\right\rangle, \tag{1.7}$$

is the anti-bonding combination of S-like orbitals of anion and cation and is the most important state for the ISB transitions and thus plays the paramount role in
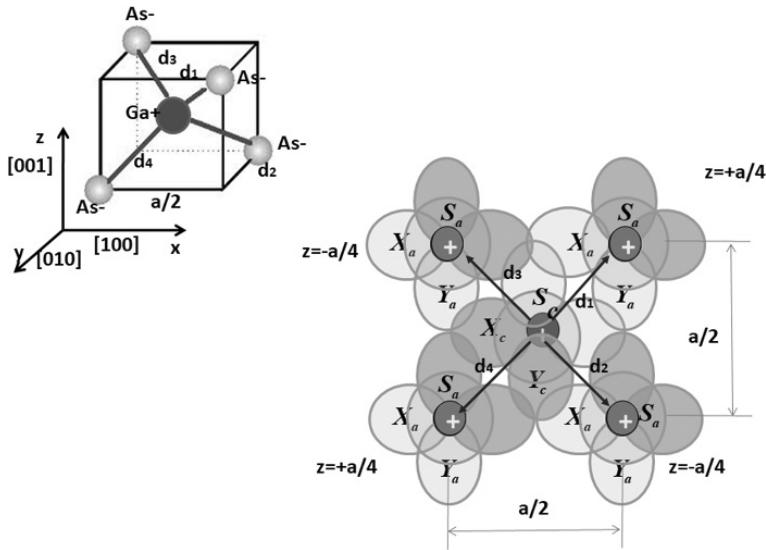
**Fig. 1.4**  Binding between basis states in the zinc-blende lattice near the center of the Brillouin zone.
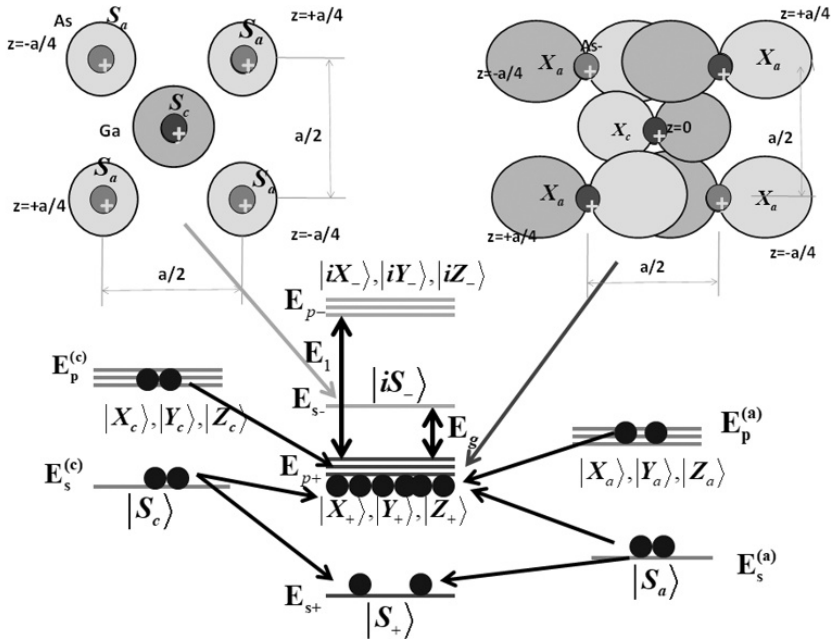


**Fig. 1.5**  Energy and composition of states in zinc-blende lattice near the center of the Brillouin zone.

QCL operation. The factor of $i$ has been introduced for convenience as shown below.

- Finally, there are three higher lying degenerate CB states with energy $E_{p+} = E_1 \sim 5 - 7$ eV:

$$u_{c2}(0) = \left| iX_- \right\rangle = i\beta \left| X_a \right\rangle - i\alpha \left| X_c \right\rangle,$$

$$u_{c3}(0) = \left| iY_- \right\rangle = i\beta \left| Y_a \right\rangle - i\alpha \left| Y_c \right\rangle, \tag{1.8}$$

$$u_{c4}(0) = \left| iZ_- \right\rangle = i\beta \left| Z_a \right\rangle - i\alpha \left| Z_c \right\rangle.$$

These states play a rather insignificant role for ISB transitions, and their impact is mostly relevant to the bulk dielectric and nonlinear optical properties.

Nevertheless, we shall keep these states for the time being.

### 1.1.2     k.P Theory Applied to Zinc Blende Semiconductors near the Brillouin Zone Center

To find the states near the center of the Brillouin zone one invokes **k.P** theory [17, 18], which seeks to express the states with small **k** as a linear combination of known states with $\mathbf{k} = \mathbf{0}$, i.e.,

$$\Psi(\mathbf{k}, \mathbf{r}) = u(\mathbf{k})e^{i\mathbf{k}\cdot\mathbf{r}} = \sum_{m=1}^{M} C_m(\mathbf{k})u_m(0, \mathbf{r})e^{i\mathbf{k}\cdot\mathbf{r}}, \tag{1.9}$$

where the summation index goes through all the bands, but in practice is always limited only to the states whose energies are not far from the energies of band edges, in our case to just the seven states described above. If one now substitutes (1.9) into the Schrödinger equation

$$\left[ -\frac{\hbar^2}{2m_0} \nabla^2 - U(\mathbf{r}) \right] \Psi = E\Psi, \tag{1.10}$$

then uses the fact that the functions $u_m(0, \mathbf{r})$ are orthogonal, and that

$$\left[ -\frac{\hbar^2}{2m_0} \nabla^2 + U(\mathbf{r}) \right] u_m(0, \mathbf{r}) = E_m u_m(0, \mathbf{r}), \tag{1.11}$$

one obtains a system of equations for the coefficients $C_m(\mathbf{k})$:

$$C_m(E_m - E + \frac{\hbar^2}{2m_0}) + \sum_{n \neq m}^{M} C_n \frac{i\hbar}{m_0} \mathbf{k} \cdot \mathbf{P}_{mn} = 0, \tag{1.12}$$

where the matrix element of the momentum between two states $m$ and $n$ is

$$\mathbf{P}_{mn} = -i\hbar \langle u_m(0)| \nabla |u_m(0)\rangle. \tag{1.13}$$

The main matrix element of interest to ISB transitions is that between the lowest anti-bonding state in the conduction band (Fig. 1.6) and one of the top states in the valence band:

$$i\hbar \langle iS_- | \nabla |X_+\rangle = P\hat{\mathbf{x}}, \tag{1.14}$$

where $P$ is a real number and $\hat{\mathbf{x}}$ is a unity vector along the [100] direction, with similar expressions for two other directions. The value of this matrix element is roughly the
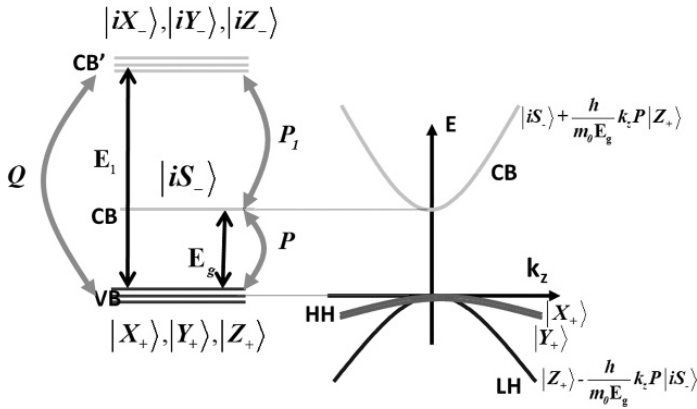
**Fig. 1.6** Energy and dispersion near the center of the Brillouin zone in the k.P model without spin-orbit interaction.

same for all III-V materials, which simply follows from the fact that the absolute value of the derivative should be on the scale of the ionic radii of cations and anions (i.e., somewhat on the order of $(\text{Å})^{-1}$ for most of the ions). Indeed, the values of this matrix element are usually quoted for the sake of convenience as follows:

$$E_P = 2P^2/m_0, \tag{1.15}$$

where $E_P$ ranges from 20 to 30 eV for all relevant semiconductors [19].

Another important matrix element connects the bonding and anti-bonding P-like states, for instance:

$$i\hbar \langle iY_- | \nabla | Z_+ \rangle = Q\hat{\boldsymbol{x}}. \tag{1.16}$$

This matrix element $Q$, usually given as $E_Q = 2Q^2/m_0$, is of the same order as $P$ and is responsible for most of the dielectric properties of III-V semiconductors. But since the upper conduction bands are separated from the states in the lowest conduction band by as much as a few eV, their impact on ISB transitions is limited – all these states are doing is providing effective mass for heavy-hole states in the valence band. In addition, due to the lack of central symmetry there exists an additional matrix element between nominally anti-bonding S-like and P-like states,

$$i\hbar \langle iS_+ | \nabla | iX_+ \rangle = iP_1\hat{\boldsymbol{x}}, \tag{1.17}$$

where $P_1 \approx (\alpha^2 - \beta^2)P$, which is responsible for all the second-order nonlinear effects, including second-harmonic generation and Pockels effect, but plays very limited role for intersubband transitions, mostly by slightly affecting all the effective masses of the electrons. If we now write the full k.P Hamiltonian for the energies that are close to the upper edge of the valence band, we obtain the following matrix in the basis of states $|iS_-\rangle, |Z_+\rangle, |X_+\rangle, |Y_+\rangle$:

$$\begin{pmatrix} E_g + \hbar^2 k^2/2m_0 & (\hbar/m_0)\,k_z P & 0 & 0 \\ (\hbar/m_0)\,k_z P & \hbar^2 k^2/2m_0 & 0 & 0 \\ 0 & 0 & \hbar^2 k^2/2m_0 - \hbar^2 k_z^2 Q^2/m_0^2 E_1 & 0 \\ 0 & 0 & 0 & \hbar^2 k^2/2m_0 - \hbar^2 k_z^2 Q^2/m_0^2 E_1 \end{pmatrix}.$$
(1.18)

In this approximation, which disregards the spin, the lowest conduction band state $|iS_-\rangle$ couples with the light state in the VB $|Z_+\rangle$, while two other states in the valence band do not couple with the conduction band and are considered to be "heavy" with effective mass $m_h^{-1} \sim m_0^{-1}(1 - E_Q/E_1)$. One can then write the characteristic equation for the conduction and light-hole states as follows:

$$\begin{vmatrix} E_g + \hbar^2 k^2/2m_0 - E(k) & (\hbar/m_0)\,k_z P \\ (\hbar/m_0)\,k_z P & \hbar^2 k^2/2m_0 - E(k) \end{vmatrix} = 0.$$
(1.19)

The equation has two solutions – for the CB:

$$E_c(k) \approx E_g + \frac{\hbar^2 k^2}{2m_0} + \frac{\hbar^2 k^2}{2m_0}\frac{E_P}{E_g} = E_g + \frac{\hbar^2 k^2}{2m_c},$$
(1.20)

and for the light valence band:

$$E_l(k) \approx \frac{\hbar^2 k^2}{2m_0} - \frac{\hbar^2 k^2}{2m_0}\frac{E_P}{E_g} = -\frac{\hbar^2 k^2}{2m_l},$$
(1.21)

where we have introduced the effective masses of the electron and light hole as

$$\begin{aligned} m_c^{-1} &= m_0^{-1}\left(E_P/E_g + 1\right), \\ m_l^{-1} &= m_0^{-1}\left(E_P/E_g - 1\right), \end{aligned}$$
(1.22)

which can be substantially smaller than the effective mass of the free electron. For instance, the effective mass of the electron for GaAs is $m_c = 0.067m_0$ and for the light hole $m_c = 0.086m_0$. At the same time, since energy $E_1 >> E_g$, the effective mass of the heavy hole is much larger, $m_h = 0.44m_0$.

Substituting solution (1.20) into (1.19) immediately gives us the coefficient $C$ that describes the admixing of the light VB state $|Z_+\rangle$ into the conduction band, and thus we obtain the overall expression for the wavefunction in the CB for small wave vectors:

$$\Psi_c(k_z, \boldsymbol{r}) = \left[ |iS_-\rangle + \frac{\hbar}{m_0 E_g} k_z P |Z_+\rangle \right] e^{ik_z z}.$$
(1.23)

It is instructive here to estimate the momentum of the state in the conduction band:

$$\langle \Psi_c^*(\boldsymbol{k}) | \boldsymbol{p} | \Psi_c(\boldsymbol{k}) \rangle = \hbar \boldsymbol{k} + \frac{2\hbar k P^2}{m_0 E_g} = \hbar \boldsymbol{k} \frac{m_0}{m_c}.$$
(1.24)

This result explains why $\hbar \boldsymbol{k}$ is called quasi-momentum and only represents a small part of the total momentum coming from the propagation term $\exp(ik_z z)$, while most of the total momentum originates from the band-mixing.
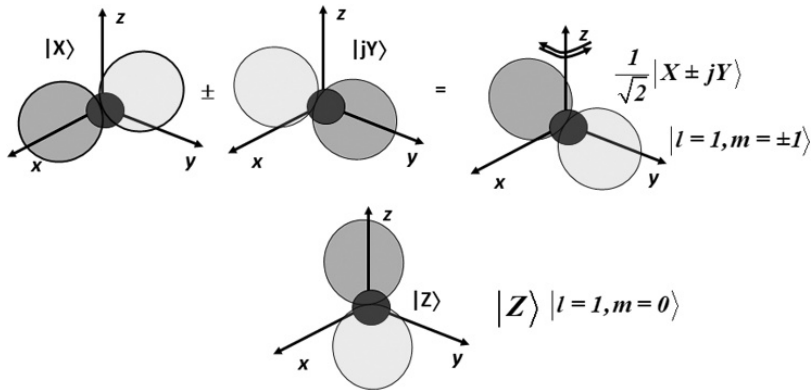
**Fig. 1.7** Basis states of the valence band with spin-orbit interaction.

### 1.1.3 Spin-Orbit Interaction and Band-Mixing in Bulk Semiconductors

The results obtained below give a good physical picture of the origin of the states in the CB with small wavevectors – there are mostly anti-bonding S-type states with the admixture of the bonding P-like states oriented along the direction of the wavevector. But in order to obtain a full picture, one must consider spin $S$ and orbital $L$ angular momenta which add up to make up a total angular momentum $J = L + S$ that must be conserved, i.e., each state must be an eigenstates with well-defined $J$. The orbital momentum of all P-like states is $l = 1$ and since spin angular momentum of 1/2 can be either parallel or anti-parallel to orbital momentum $J$ can take values of $^1/_2$ or 3/2. One can re-arrange six (including spin) wavefunctions in the VB and label them by their orbital angular momentum, its projection on the $z$-axis, $m$ (see Fig 1.7), the spin projection onto the same axis, $m_\mathrm{s}$, and the projection of total angular momentum, $m_J$ [12, 18]:

$$\frac{1}{\sqrt{2}}|X_+ + iY_+\rangle \uparrow = \left| m = 1, m_\mathrm{s} = \frac{1}{2}, m_J = \frac{3}{2} \right\rangle,$$

$$|Z_+\rangle \uparrow = \left| m = 0, m_\mathrm{s} = \frac{1}{2}, m_J = \frac{1}{2} \right\rangle,$$

$$\frac{1}{\sqrt{2}}|X_+ + iY_+\rangle \downarrow = \left| m = 1, m_\mathrm{s} = -\frac{1}{2}, m_J = \frac{1}{2} \right\rangle,$$

$$\frac{1}{\sqrt{2}}|X_+ - iY_+\rangle \uparrow = \left| m = -1, m_\mathrm{s} = \frac{1}{2}, m_J = -\frac{1}{2} \right\rangle, \tag{1.25}$$

$$|Z_+\rangle \downarrow = \left| m = 0, m_s = -\frac{1}{2}, m_J = -\frac{1}{2} \right\rangle,$$

$$\frac{1}{\sqrt{2}}|X_+ - iY_+\rangle \downarrow = \left| m = -1, m_\mathrm{s} = -\frac{1}{2}, m_J = -\frac{3}{2} \right\rangle.$$

Two states with projection of total angular momentum $m_J = \pm 3/2$ are already the eigenstates of $J$ with $J = 3/2$, while the four states with $m_J = \pm 1/2$ can be states with

either $J = 1/2$ or $J = 3/2$; and therefore they get mixed by the spin-orbit interaction Hamiltonian:

$$H_{so} = \frac{eE_r}{2m_0^2 c^2 r} \boldsymbol{L} \cdot \boldsymbol{S}, \tag{1.26}$$

where $E_r$ is the field that attracts the electron to the nucleus, which increases with increasing atomic number. Therefore, the energies of states with parallel angular and spin momenta increase by

$$\left\langle m = \pm 1, m_s = \pm \frac{1}{2} \middle| H_{so} \middle| m = \pm 1, m_s = \pm \frac{1}{2} \right\rangle = \frac{\Delta}{3}, \tag{1.27}$$

where $\Delta$ is a spin-orbit splitting energy (for GaAs $\Delta = 0.4\,\text{eV}$), while energies of states with anti-parallel angular and spin momenta decrease by the same amount:

$$\left\langle m = \mp 1, m_s = \pm \frac{1}{2} \middle| H_{so} \middle| m = \mp 1, m_s = \pm \frac{1}{2} \right\rangle = -\frac{\Delta}{3}, \tag{1.28}$$

and the states with the same projection of total angular momentum $m_J$ get mixed:

$$\left\langle m = 0, m_s = \mp \frac{1}{2} \middle| H_{so} \middle| m = \mp 1, m_s = \pm \frac{1}{2} \right\rangle = \frac{\sqrt{2}\Delta}{3}. \tag{1.29}$$

Hence in the basis of $\left| m = \pm 1, m_s = \pm \frac{1}{2} \right\rangle$, $\left| m = 0, m_s = \pm \frac{1}{2} \right\rangle$, and $\left| m = \pm 1, m_s = \mp \frac{1}{2} \right\rangle$ the spin-orbit Hamiltonian can be written in matrix form as follows:

$$H_{so} = \begin{pmatrix} \Delta/3 & 0 & 0 \\ 0 & 0 & \sqrt{2}\Delta/3 \\ 0 & \sqrt{2}\Delta/3 & -\Delta/3 \end{pmatrix}, \tag{1.30}$$

and the characteristic equation for energy becomes

$$\begin{vmatrix} \Delta/3 - E & 0 & 0 \\ 0 & -E & \sqrt{2}\Delta/3 \\ 0 & \sqrt{2}\Delta/3 & -\Delta/3 - E \end{vmatrix} = 0. \tag{1.31}$$

This equation has three solutions, as shown in Fig. 1.8(a).
The original heavy-hole state with energy $\Delta/3$:

$$\left| J = \frac{3}{2}, m_J = \pm \frac{3}{2} \right\rangle = \frac{1}{\sqrt{2}} |X_+ \pm iY_+\rangle \uparrow\downarrow. \tag{1.32}$$

The light-hole state also with energy $\Delta/3$:

$$\left| J = \frac{3}{2}, m_J = \pm \frac{1}{2} \right\rangle = \sqrt{\frac{2}{3}} |Z_+\rangle \uparrow\downarrow - \frac{1}{\sqrt{6}} |X_+ \pm iY_+\rangle \downarrow\uparrow, \tag{1.33}$$

which is technically 2/3 light and 1/3 heavy state, and a split-off band with energy $-2\Delta/3$:

$$\left| J = \frac{1}{2}, m_J = \pm \frac{1}{2} \right\rangle = \frac{1}{\sqrt{3}} |Z_+\rangle \uparrow\downarrow + \frac{1}{\sqrt{3}} |X_+ \pm iY_+\rangle \downarrow\uparrow, \tag{1.34}$$
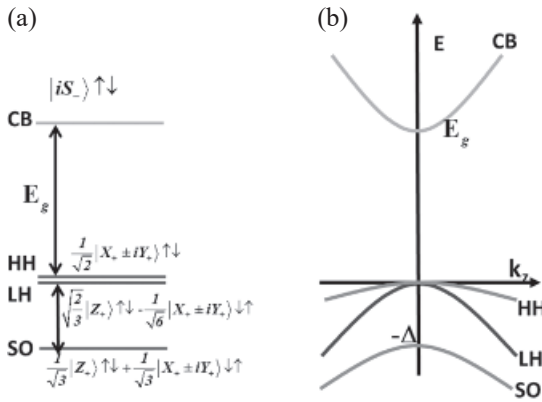
(a)

(b)



**Fig. 1.8** Energy band composition and dispersion near the center of the Brillouin zone in the **k.P** model with spin-orbit interaction.

which is technically 1/3 light and 2/3 heavy state. The heavy-hole state is not being mixed into the conduction-band states, but both light-hole and split-off hole states do, so we can rewrite the characteristic equation (1.19), for the three-band k.P Hamiltonian, in the basis $u_1 = |iS_- \uparrow\downarrow\rangle$, $u_2 = |Z_+ \uparrow\downarrow\rangle$, and $u_3 = 2^{-1/2}|(\pm X_+ + iY_+) \downarrow\uparrow\rangle$ as follows:

$$
\begin{vmatrix}
E_{\mathrm{g}} + \dfrac{\hbar^2 k^2}{2m_0} - E(k) & (\hbar/m_0)\, k_z P & 0 \\[3mm]
(\hbar/m_0)\, k_z P & \dfrac{\hbar^2 k^2}{2m_0} - \dfrac{1}{3}\Delta - E(k) & \dfrac{\sqrt{2}}{3}\Delta \\[3mm]
0 & \dfrac{\sqrt{2}}{3}\Delta & \dfrac{\hbar^2 k^2}{2m_0} - \dfrac{2}{3}\Delta - E(k)
\end{vmatrix} = 0. \quad (1.35)
$$

If we now consider the state in the CB with a small wavevector, and substitute $E(k) \approx E_{\mathrm{g}}$ into the last two lines, we immediately obtain

$$
E_{\mathrm{c}}(k) \approx E_{\mathrm{g}} + \frac{\hbar^2 k^2}{2m_0} + \frac{\hbar^2 k^2}{2m_0} \frac{E_{\mathrm{P}}(E_{\mathrm{g}} + 2\Delta/3)}{E_{\mathrm{g}}(E_{\mathrm{g}} + \Delta)} = E_{\mathrm{g}} + \frac{\hbar^2 k^2}{2m_c}, \quad (1.36)
$$

which is shown in Fig. 1.8(b), where the effective mass is

$$
m_{\mathrm{c}}^{-1} = m_0^{-1} \left( \frac{E_{\mathrm{P}}(E_{\mathrm{g}} + 2\Delta/3)}{E_{\mathrm{g}}(E_{\mathrm{g}} + \Delta)} + 1 \right). \quad (1.37)
$$

In comparison to (1.22) the effective mass is changed by spin-orbit interaction rather insignificantly, but as we shall soon see the spin-orbit interaction becomes important when it comes to optical properties.

### 1.1.4   States in Quantum Wells in the Envelope Approximation

We now consider a semiconductor QW consisting of a narrow bandgap material layer, such as GaAs or InGaAs surrounded by higher bandgap material (AlGaAs or InP)
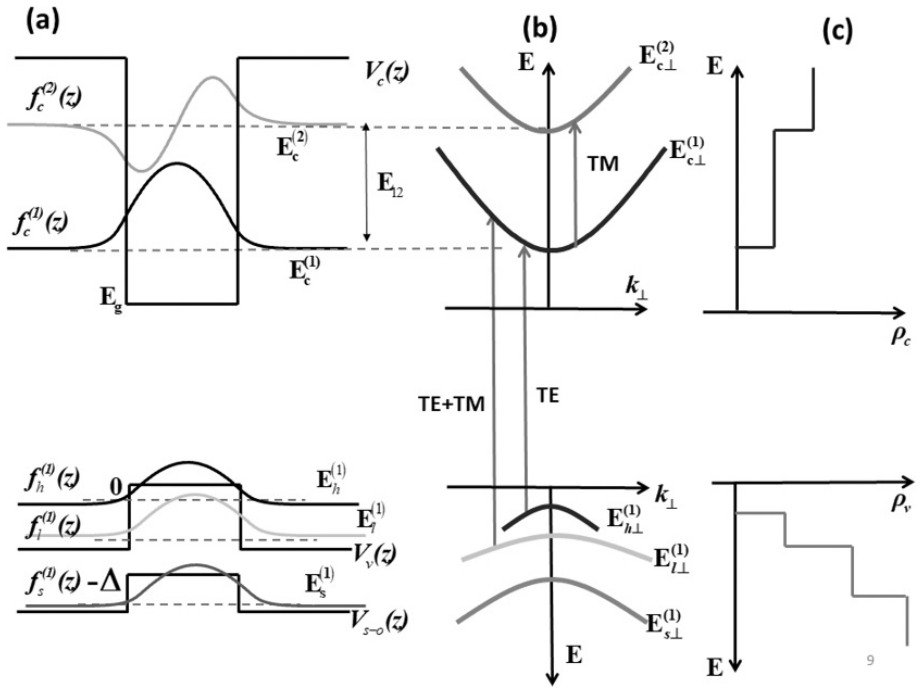
**Fig. 1.9** (a) QW subband energies and envelope wavefunctions, (b) in-plane dispersion with optical transitions for TE and TM polarized light, and (c) density of states.

as shown in Fig. 1.9(a). The confining potential can be described as $V_c(z)$ and the wavefunction of the $m$th state (subband) in the CB can be written as follows [12]:

$$\Psi_c^m(\boldsymbol{k}_\perp, \boldsymbol{r}) = \sum_{n=1}^{3} f_n^{(m)}(z) u_n(\boldsymbol{r}) e^{i\boldsymbol{k}_\perp \cdot \boldsymbol{r}_\perp}, \tag{1.38}$$

where $f_n^m$ is the envelope function describing the contribution of the $n$th basis state in (1.35); i.e., $n = c, l, s$ for the conduction, light-hole, and split-off bands, respectively, to the state in the $m$th subband in the QW, and $\boldsymbol{k}_\perp$ and $\boldsymbol{r}_\perp$ are the wave vector and coordinate in the QW plane $xy$. The wavefunctions are shown in Fig. 1.9(a). Substituting this into the original wave equation we obtain

$$\left[ -\frac{\hbar^2}{2m_0} \nabla^2 + U(\boldsymbol{r}) + V_c(z) \right] \Psi_c^m(\boldsymbol{k}_\perp, \boldsymbol{r}) = E_c^m(\boldsymbol{k}_\perp) \Psi_c^m(\boldsymbol{k}_\perp, \boldsymbol{r}). \tag{1.39}$$

One can separate the variables into the in-plane motion with energy

$$E_{c\perp}^{(m)} = \hbar^2 k_\perp^2 / 2m_c, \tag{1.40}$$

as shown in Fig. 1.9(b), and the motion in the $z$-direction for which we substitute $\partial/\partial z$ operator in place of $ik_z$ in (1.35) and obtain the equation:

$$\begin{pmatrix} -\dfrac{\hbar^2}{2m_0}\dfrac{\partial}{\partial z} - E_{\mathrm{c}}^{(m)} + V_{\mathrm{c}}(z) & i\dfrac{\hbar}{m_0}\dfrac{\partial}{\partial z}P & 0 \\[2mm] i\dfrac{\hbar}{m_0}P\dfrac{\partial}{\partial z} & -\dfrac{\hbar^2}{2m_0}\dfrac{\partial^2}{\partial z} - \dfrac{1}{3}\Delta - E_{\mathrm{g}} - E_{\mathrm{c}}^{(m)} + V_{\mathrm{v}}(z) & \dfrac{\sqrt{2}}{3}\Delta \\[2mm] 0 & \dfrac{\sqrt{2}}{3}\Delta & -\dfrac{\hbar^2}{2m_0}\dfrac{\partial^2}{\partial z} - \dfrac{2}{3}\Delta - E_{\mathrm{g}} - E_{\mathrm{c}}^{(m)} + V_{\mathrm{s}}(z) \end{pmatrix}$$

$$\times \begin{pmatrix} f_{\mathrm{c}}^{(m)} \\[1mm] f_{\mathrm{l}}^{(m)} \\[1mm] f_{\mathrm{s}}^{(m)} \end{pmatrix} = 0, \tag{1.41}$$

where $E_{\mathrm{c}}^{(m)}$ is the energy of the $m$th conduction band, relative to the bandgap band at $k_\perp = 0$, and $V_v(z)$ and $V_s(z)$ are the potentials in the light-hole and split-off bands, respectively. Now for the state not far from the bottom of the CB one can re-write (1.41) as such:

$$\begin{pmatrix} -\dfrac{\hbar^2}{2m_0}\dfrac{\partial^2}{\partial z} + E_{\mathrm{c}}^{(m)} + V_{\mathrm{c}}(z) & i\dfrac{\hbar}{m_0}\dfrac{\partial}{\partial z}P & 0 \\[2mm] i\dfrac{\hbar}{m_0}P\dfrac{\partial}{\partial z} & -\dfrac{1}{3}\Delta - E_{\mathrm{g}} - E_{\mathrm{c}}^{(m)} & \dfrac{\sqrt{2}}{3}\Delta \\[2mm] 0 & \dfrac{\sqrt{2}}{3}\Delta & -\dfrac{2}{3}\Delta - E_{\mathrm{g}} - E_{\mathrm{c}}^{(m)} \end{pmatrix}$$

$$\times \begin{pmatrix} f_{\mathrm{c}}^{(m)} \\[1mm] f_{\mathrm{l}}^{(m)} \\[1mm] f_{\mathrm{s}}^{(m)} \end{pmatrix} = 0. \tag{1.42}$$

The last equation in (1.42) readily yields

$$f_{\mathrm{s}}^{(m)}(z) = f_{\mathrm{l(m)}}(z)\frac{\frac{\sqrt{2}}{3}\Delta}{\frac{2}{3}\Delta + E_{\mathrm{g}} + E_{\mathrm{c}}^{(m)}}, \tag{1.43}$$

and substitution of (1.43) into the second equation of (1.42) results in

$$f_{\mathrm{l}}^{(m)}(z) = i\frac{\hbar}{m_0}P\frac{\frac{2}{3}\Delta + E_{\mathrm{g}} + E_{\mathrm{c}}^{(m)}}{(E_{\mathrm{c}}^{(m)} + E_{\mathrm{g}})(E_{\mathrm{g}} + E_{\mathrm{c}}^{(m)} + \Delta)}\frac{\partial f_{\mathrm{c}}^{(m)}(z)}{\partial z} = \frac{i\hbar}{2P}\left(\frac{m_0}{m_{\mathrm{c}}(E_{\mathrm{c}}^{(m)})} - 1\right)\frac{\partial f_{\mathrm{c}}^{(m)}(z)}{\partial z}, \tag{1.44}$$

where we have introduced the **energy-dependent** effective mass of the conduction band,

$$m_{\mathrm{c}}^{-1}(E_{\mathrm{c}}^{(m)}) = m_0^{-1}\left(\frac{E_{\mathrm{P}}(E_{\mathrm{g}} + E_{\mathrm{c}}^{(m)} + 2\Delta/3)}{(E_{\mathrm{g}} + E_{\mathrm{c}}^{(m)})(E_{\mathrm{g}} + E_{\mathrm{c}}^{(m)} + \Delta)} + 1\right). \tag{1.45}$$

Since the bandgap energy changes as a function of the coordinate, the effective mass is not only energy-dependent but also coordinate dependent. Now, by substituting (1.44) into the first equation of (1.42) we obtain a Schrödinger equation,

$$-\frac{\hbar^2}{2m_{\mathrm{c}}\left(E_{\mathrm{c}}^{(m)}\right)}\frac{\partial^2 f_{\mathrm{c}}^{(m)}}{\partial z^2} + V_c(z)f_{\mathrm{c}}^{(m)} = E_{\mathrm{c}}^{(m)}f_{\mathrm{c}}^{(m)}, \tag{1.46}$$

for the CB envelope function in the energy-dependent effective-mass approximation. This equation is solved using boundary conditions requiring continuity of $f_{\mathrm{c}}^{(m)}(z)$ and

$m_c^{-1} \partial f_c^{(m)}(z)/\partial z$ and the values of subband energies $E_c^m$, shown in Fig. 1.9(b), can be determined. We can then write out the expression for the overall CB wavefunction (1.38) as follows:

$$\Psi_c^m(\boldsymbol{k}_\perp, \boldsymbol{r}) \uparrow\downarrow = \left[ f_1^m(z) \, |iS_- \uparrow\downarrow\rangle + \frac{i\hbar}{2P} \left( \frac{m_0}{m_c(E_c^m)} - 1 \right) \right.$$
$$\left. \times \frac{\partial f_1^m(z)}{\partial z} \left[ |Z_+ \uparrow\downarrow\rangle + \frac{r_\Delta}{\sqrt{2}} |(\pm X_+ + iY_+) \downarrow\uparrow\rangle \right] \right] e^{i\boldsymbol{k}_\perp \cdot \boldsymbol{r}_\perp}, \quad (1.47)$$

where

$$r_\Delta = \frac{\frac{\sqrt{2}}{3}\Delta}{\frac{2}{3}\Delta + E_g + E_c^{(m)}}. \quad (1.48)$$

Therefore the VB states get admixed into the CB in such a way that the parity of their envelope functions, $f_1^m(z)$ and $f_s^m(z)$, is opposite from the parity of the CB envelope function $f_c^m(z)$. The mixing is relatively small and can be evaluated by noting that the order of magnitude of the derivative of the envelope function is roughly $(1/d)$, where $d$ is its spatial extent. Then the relative weight of mixed-in VB states is roughly $(r_{ion}/d)^2$, where $r_{ion}$ is the ionic radius of the order of 1 Å. Therefore, the relative weight of the VB wavefunction is typically less than 0.1%. Nevertheless, as we shall see below, it is this mixing that engenders strong intersubband transitions.

## 1.2     Intersubband Transitions – Their Origin and Relative Strength

### 1.2.1     Interband Absorption in Quantum Wells

Let us evaluate the absorption coefficient between the two subbands, one in the valence band $\Psi_v^m$ (where $v$ can be either heavy (h)- or light (l)-hole subband) and one in the conduction band $\Psi_c^n$. The Hamiltonian of the interaction between electro-magnetic wave $\boldsymbol{E}(t) = \frac{1}{2}\boldsymbol{E}(\omega)\exp(i\omega t) + c.c.$ is [16]

$$H_E = \frac{e}{m_0}\boldsymbol{p} \cdot \boldsymbol{A}, \quad (1.49)$$

where $\boldsymbol{A}$ is a vector potential, related to the electric field as $\boldsymbol{E}(t) = \partial \boldsymbol{A}/\partial t$ and $\boldsymbol{p} = -i\hbar\nabla$ is a momentum operator. We shall start with Fermi's golden rule to evaluate the rate of change of the 2D carrier density due to the absorption of light as such:

$$\frac{dn_{2D}}{dt} = \frac{2\pi}{\hbar} \frac{e^2 p_{cv}^2}{m_0^2 \omega^2} \rho_{cv} \frac{E^2(\omega)}{4} F_{mn}, \quad (1.50)$$

where $p_{cv}$ is the matrix element of momentum operator between the Bloch functions of the conduction and valence bands; the $F_{mn}$ term,

$$F_{mn} = \left| \int f_c^{(n)}(z) f_v^{(m)}(z) dz \right|^2, \quad (1.51)$$

is the overlap of envelope wavefunctions, the factor of $1/4$ is related to the fact that only the positive frequencies of the electric field contribute to the absorption, and the joint density of states (Fig. 1.9(c)) is

$$\rho_{cv}^{(mn)}(\hbar\omega) = \frac{\mu_{cv}}{\pi\hbar^2}H(\hbar\omega - E_g - E_c^{(n)} - E_v^{(m)}), \tag{1.52}$$

where $H$ is the Heaviside step function, and $\mu_{cv} = \left(m_c^{-1} + m_{v,|\perp}^{-1}\right)^{-1}$ is the reduced mass. Before continuing it is important to note that the in-plane valence band effective masses in QWs are different from their bulk values, namely $m_{hh,|\perp}^{-1} = \frac{3}{4}m_{lh}^{-1} + \frac{1}{4}m_{hh}^{-1}$ and $m_{lh,|\perp}^{-1} = \frac{3}{4}m_{hh}^{-1} + \frac{1}{4}m_{lh}^{-1}$ .

Let us first consider the interband transition between the heavy-hole subband and the conduction band, for which the matrix element can be found as follows:

$$\boldsymbol{p}_{12} = \langle -iS \uparrow\downarrow |\boldsymbol{p}| \frac{1}{\sqrt{2}} |(\pm X_+ + iY_+) \uparrow\downarrow\rangle = \frac{P}{\sqrt{2}}(\pm\hat{\boldsymbol{x}} + i\hat{\boldsymbol{y}}). \tag{1.53}$$

For linearly polarized light we obtain $p_{cv}^2 = P^2/2 = m_0 E_P/4$. At the same time, we can pay attention to (1.45) and note that $m_c^{-1} \sim m_0^{-1} + 2P^2/m_0^2 E_g$. Since the effective mass of a hole is always higher than that of an electron, the reduced mass should be of the order of $\mu_{cv} \sim m_0 E_g/E_P$, and one can introduce a dimensionless parameter:

$$R_{cv} = \frac{E_P}{m_0 E_g}\mu_{cv}, \tag{1.54}$$

which is on the order of unity for most III-V semiconductors (for instance, for GaAs $m_c = 0.67m_0$, in-plane $m_{hh,\perp} = 0.11m_0$, $\mu_{cv} = 0.041m_0$, and $E_P = 28.8$ eV we get $R_P = 0.82$). Therefore, from (1.52) $\rho_{cv} = R_{cv}m_0 E_g/E_P\pi\hbar^2$ and under the assumption that $\hbar\omega \sim E_{gap}$ and by introducing the power density of light propagating in the direction normal to the plane of QWs (Fig. 1.10(a)):

$$I_\omega = \frac{n_r}{2\eta_0}E(\omega)^2, \tag{1.55}$$

where $n_r$ is the refractive index and $\eta_0 = 377\Omega$ is the vacuum impedance, one obtains from (1.50) the expression for the rate of increase of the energy density inside QWs as such:

$$\frac{du_{2D}}{dt} = \hbar\omega\frac{dn_{2D}}{dt} = \hbar\omega\frac{2\pi}{\hbar}\frac{e^2}{m_0^2\omega^2}\frac{m_0 E_P}{4}R_{ch}\frac{m_0 E_g}{E_P\pi\hbar^2}\frac{\eta_0 I_\omega}{2n_r}F_{mn}$$
$$= \frac{\eta_0 e^2}{4\hbar n_r}R_{ch}F_{mn}I_\omega = \alpha_{ch}^{(mn)}(\omega)I_\omega, \tag{1.56}$$

where the absorption coefficient per one QW between the $m$th heavy-hole subband and $n$th conduction band subband is a remarkably simple expression:

$$\alpha_{ch}^{(mn)} = \frac{\pi\alpha_0}{n_r}R_{ch}F_{mn}, \tag{1.57}$$

where $\alpha_0 = 1/137$ is the fine structure constant, indicating that practically any semiconductor 2D structure has an absorption coefficient per one layer on the order of 1%.
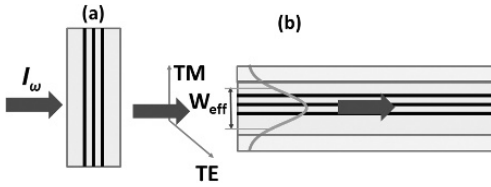
**Fig. 1.10** (a) Absorption for normal incidence light; (b) TE and TM absorption for the waveguide propagation.

If, on the other hand, one considers the propagation of the light in the dielectric waveguide mode (Fig. 1.10(b)) defined by the effective width $W_{\text{eff}}$ and containing $N_{\text{QW}}$, the number of quantum wells, the absorption will take place only for the TE (in-plane) polarized light and the absorption coefficient (now per unit of length) will be

$$\alpha_{\text{ch}}^{\text{TE}} = N_{QW}\alpha_{\text{ch}}^{(mn)} = N_{\text{QW}}\frac{\pi\alpha_0}{n_{\text{r}}W_{\text{eff}}}R_{\text{ch}}F_{mn}, \tag{1.58}$$

while the absorption of the TM waves will be zero.

For the transition between the light-hole VB and CB the momentum matrix element is given by

$$p_{cl} = \langle iS \uparrow\downarrow |\boldsymbol{p}| \sqrt{\frac{2}{3}} |Z_+ \uparrow\downarrow\rangle - \langle iS \uparrow\downarrow |\boldsymbol{p}| \frac{1}{\sqrt{6}} |(\pm X_+ + iY_+) \downarrow\uparrow\rangle$$

$$= \sqrt{\frac{2}{3}}P\hat{\boldsymbol{z}} - \frac{P}{\sqrt{6}}(\pm\hat{\boldsymbol{x}} + i\hat{\boldsymbol{y}}). \tag{1.59}$$

Therefore, for the in-plane polarization the absorption coefficient of the light hole to the conduction band will be

$$\alpha_{cl}^{\text{TE}} = \frac{1}{3}N_{\text{QW}}\frac{\pi\alpha_0}{n_{\text{r}}W_{\text{eff}}}R_{cl}F_{mn} \approx \frac{1}{3}\alpha_{\text{ch}}^{\text{TE}}, \tag{1.60}$$

while for the TM polarization, normal to the QW plane, the light-hole state is expected to absorb very strongly:

$$\alpha_{cl}^{\text{TM}} = \frac{4}{3}N_{\text{QW}}\frac{\pi\alpha_0}{n_{\text{r}}W_{\text{eff}}}R_{cl}F_{mn} \approx \frac{4}{3}\alpha_{\text{ch}}^{\text{TE}}. \tag{1.61}$$

Of course, absorption of TM polarized light can only be observed if the incident light impinges onto a surface at an oblique angle, or, better in the waveguide geometry of Fig. 1.10(b).

### 1.2.2     Band-mixing Origin of ISB Transitions

Let us now turn our attention to our main subject – intersubband absorption. We now must evaluate the matrix element between two states described by (1.47) with $m = 1, 2$. First, let us consider the matrix element for the light that is TM (or normal to the QW plane) polarized:
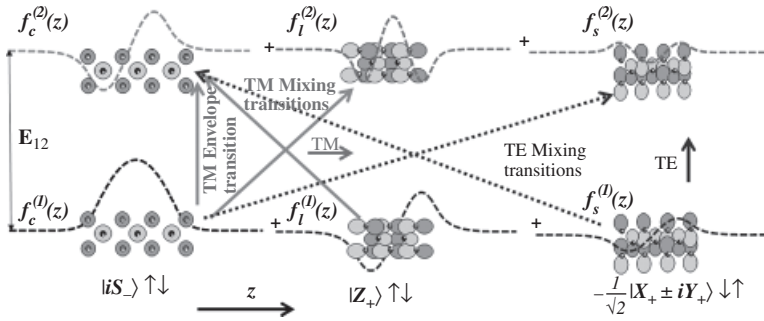
**Fig. 1.11** Composition of the states in the subbands and the origin of TM and TE transitions between the subbands.

$$
p_{12,z} = -i\hbar \left[ \left\langle -iS_- \uparrow \middle| f_c^{(1)} - \frac{i\hbar}{2P} \left( \frac{m_0}{m_c(E_c^{(1)})} - 1 \right) \frac{\partial f_c^{(1)}}{\partial z} \left\langle Z \uparrow \middle| \right]
$$

$$
\times \left[ \middle| iS_- \uparrow \right\rangle \frac{\partial f_c^{(2)}}{\partial z} + f_c^{(2)} \frac{\partial}{\partial z} \middle| iS_- \uparrow \right\rangle + \frac{i\hbar}{2P} \left( \frac{m_0}{m_c(E_c^{(2)})} - 1 \right) \frac{\partial f_c^{(2)}}{\partial z} \middle| Z \uparrow \right\rangle \right]
$$

$$
= -i\hbar \left[ \int f_c^{(1)} \frac{\partial f_c^{(2)}}{\partial z} dz - \frac{1}{2} \left( \frac{m_0}{m_c(E_c^{(1)})} - 1 \right) \int f_c^{(2)} \frac{\partial f_c^{(1)}}{\partial z} dz \right.
$$

$$
\left. + \frac{1}{2} \left( \frac{m_0}{m_c(E_c^{(2)})} - 1 \right) \int f_c^{(1)} \frac{\partial f_c^{(2)}}{\partial z} dz \right].
\tag{1.62}
$$

The first term is an "envelope contribution" while the second and third terms are the contributions due to band-mixing, which turns out to be the dominant contribution to the strength of transition. This is explained in Fig. 1.11 where it is shown how k.P interaction mixes the light and split-off states into conduction subbands. For the two bands that are relatively close to each other, one can assume some average effective mass $\overline{m}_c^* = m_c(E_c^{(2)} + E_c^{(1)})/2$ and substitute it into (1.62) to obtain

$$
p_{12,z} = -i\hbar \frac{m_0}{m_c} \int f_c^{(1)} \frac{\partial f_c^{(2)}}{\partial z} dz = \frac{m_0}{m_c} p_{12,z}^*,
\tag{1.63}
$$

where

$$
p_{12,z}^* = -i\hbar \int f_c^{(1)} \frac{\partial f_c^{(2)}}{\partial z} dz
\tag{1.64}
$$

is a "quasi-momentum" matrix element of envelope wavefunctions, estimated without taking into account the increase caused by band-mixing. As one can see, band-mixing leads to a very large increase in the matrix element of the momentum for the ISB transition, similar to the one described by the expression (1.24) for the momentum of the electron in the conduction band. We can also find the matrix element of the coordinate of the intersubband transition,

$$z_{12} = \frac{p_{12}}{m_0 \omega_{21}} = -i\hbar \frac{1}{m_c \omega_{21}} \int f_c^{(1)} \frac{\partial f_c^{(2)}}{\partial z} dz = \int f_c^{(1)} z f_c^{(2)} dz, \qquad (1.65)$$

which indicates that one can estimate the transition strength using the standard definition of the moment of the coordinate, but without the derivation performed in this chapter the band-mixing origin [6, 20] of the "giant" ISB transition strength would not have been revealed.

The per-well absorption coefficient for the ISB transition can be inferred from the one for the interband transitions (1.56) by simply using a different effective density of states,

$$\rho_{12}(\hbar\omega) = \frac{1}{\pi} \frac{\Gamma}{(E_{21} - \hbar\omega)^2 + \Gamma^2}, \qquad (1.66)$$

where $N_{2D}$ is two-dimensional density of carriers and $\Gamma$ is broadening of the ISB transition to obtain

$$\alpha_{12}^{TM}(\omega) = \frac{\alpha}{W_{eff}} \frac{N_{QW}}{\hbar} \hbar\omega \frac{2\pi}{\hbar} \frac{e^2 p_{12}^2}{m_0^2 \omega^2} \frac{N_{2D}\Gamma}{(E_{21} - \hbar\omega)^2 + \Gamma^2} \frac{\eta_0}{2n_r}, \qquad (1.67)$$

where $N_{2D}$ is two-dimensional carrier density. At resonance $\omega = \omega_{21}$; thus, the absorption amounts to

$$\alpha_{12}^{TM}(\omega_{12}) = \frac{N_{QW}}{W_{eff}} \frac{4\pi\alpha_0}{n_r} \frac{\hbar N_{2D} |p_{12}^*|^2}{\omega_{21} m_0^2 \Gamma} = \frac{4\pi\alpha_0}{n_r} \frac{\hbar\omega_{12}}{\Gamma} \frac{N_{QW} N_{2D}}{W_{eff}} z_{12}^2. \qquad (1.68)$$

Next, we can evaluate the strength of the transition for TE (or in-plane) polarized light. Since the heavy-hole like state $|2^{-1/2} (X_+ \pm iY_+) \downarrow\uparrow\rangle$ gets mixed into the conduction band with the opposite spin, the matrix element of in-plane momentum becomes [20, 21]:

$$\begin{aligned}
p_{12,x} &= -i\hbar \left[ \langle -iS_- \uparrow| f_c^{(1)} - \frac{i\hbar}{2P} \left( \frac{m_0}{m_c(E_c^{(1)})} - 1 \right) \frac{r_{\Delta 1}}{\sqrt{2}} \frac{\partial f_c^{(1)}}{\partial z} \langle (X - jY) \downarrow| \right] \\
&\quad \times \left[ f_c^{(2)} \frac{\partial}{\partial z} |iS_- \downarrow\rangle + \frac{i\hbar}{2P} \left( \frac{m_0}{m_c(E_c^{(2)})} - 1 \right) \frac{r_{\Delta 2}}{\sqrt{2}} \frac{\partial f_c^{(2)}}{\partial z} |(-X + jY) \uparrow\rangle \right] \\
&= -i\hbar \left[ -\frac{r_{\Delta 1}}{2^{3/2}} \left( \frac{m_0}{m_c(E_c^{(1)})} - 1 \right) \int f_c^{(2)} \frac{\partial f_c^{(1)}}{\partial z} dz \right. \\
&\quad \left. -\frac{r_{\Delta 2}}{2^{3/2}} \left( \frac{m_0}{m_c(E_c^{(2)})} - 1 \right) \int f_c^{(1)} \frac{\partial f_c^{(2)}}{\partial z} dz \right] \\
&= -\frac{i\hbar}{2^{3/2}} \int f_c^{(2)} \frac{\partial f_c^{(1)}}{\partial z} dz \left[ r_{\Delta 2} \left( \frac{m_0}{m_c(E_c^2)} - 1 \right) - r_{\Delta 1} \left( \frac{m_0}{m_c(E_c^{(1)})} - 1 \right) \right].
\end{aligned} \qquad (1.69)$$

As one can see, the matrix element for intersubband in-plane transition is significantly smaller than that for normal-to-plane polarization. This happens precisely because the transition must involve spin flip and would have been entirely forbidden if not for

spin-orbit interaction. Using (1.48) one can obtain an approximate relation between the two:

$$\frac{p_{12,x}}{p_{12,z}} \approx \frac{\sqrt{2}\Delta\left(E_c^{(2)} - E_c^{(1)}\right)}{3E_g^2}.$$ (1.70)

Therefore, TE-polarized wave absorption between subbands is very weak in most relevant semiconductor QWs, with the possible exception of antimonides, in which case the bandgap energy and spin-orbit splitting energy are of the same magnitude. However, that does not mean that doped QWs do not absorb the TE-polarized light – this absorption is called free-carrier absorption and shall be considered next.

### 1.2.3 Free-Carrier Absorption and Its Relation to ISB Transitions

Free-carrier absorption occurs for the light polarized in the plane of the QWs (Fig. 1.12). For the absorption to take place between two states, one near the bottom of subband with $k_{\perp 1} = 0$ and one with $k_{\perp 2} > 0$, it is necessary to conserve both energy and momentum. Momentum conservation usually involves scattering by either a phonon or an imperfection, such as surface roughness. The matrix element of the scattering Hamiltonian $H_{scat}(k_{\perp 2})$ in general depends on the absolute value of in-plane wavevector $k_\perp$ ; i.e., on the energy:

$$E_2 - E_1 = \hbar^2 k_\perp^2 / 2m_c = \hbar\omega.$$ (1.71)

Essentially free-carrier absorption is a two-step process in which the electron from the bottom of subband scatters into the virtual state with wavevector $k_{\perp 2}$ and with energy $\pm E_{ph}$, which can be positive or negative, depending on whether the phonon is absorbed or emitted, or zero for all the elastic-scattering processes. Usually $E_{ph} << \hbar\omega$ and can be neglected, unless, of course, one is dealing with nitrides for which the LO–phonon energy is 90 meV, and thus comparable to the energy of the ISB transition itself. The scattering process is followed by the absorption of the phonon with energy $\hbar\omega$, and
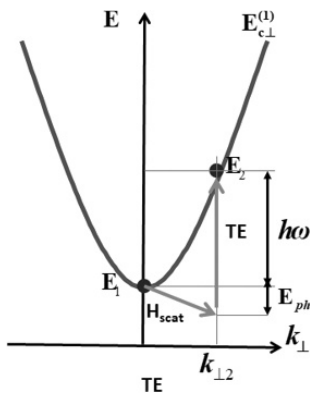


**Fig. 1.12** Origin of free-carrier absorption in doped semiconductor QWs.

the interaction Hamiltonian $e\boldsymbol{p} \cdot \boldsymbol{A}/m_0$, where the momentum of the electron in state $\boldsymbol{k}_{\perp 2}$ is given by (1.23). Therefore $\langle e\boldsymbol{p} \cdot \boldsymbol{A}/m_0 \rangle_{22} = e\hbar \boldsymbol{k}_{\perp 2} \cdot \boldsymbol{E}/m_c\omega$, and one can write for the rate of absorption from a given state near $\boldsymbol{k}_{\perp 1} = 0$, by using the Fermi golden rule,

$$R_{\text{abs}}(\omega) = \frac{2\pi}{\hbar} \frac{|H_{\text{scat}}(\omega)|^2}{\hbar^2\omega^2} \frac{e^2 E_\perp^2}{4\omega^2} \frac{\hbar^2 k_{\perp 2}^2 \langle \cos^2\theta \rangle}{m_c^2} \frac{1}{2}\rho_c, \tag{1.72}$$

where $E_\perp$ is the in-plane (TE) component of the electric field, and $\rho_c = m_c/\pi\hbar^2$ is the density of states in the CB (the factor $1/2$ in front of it indicates that the scattering processes typically preserve the spin) and $\theta$ is the angle between $\boldsymbol{k}_{\perp 2}$ and the polarization of the electric field – obviously the mean value $\langle \cos^2\theta \rangle = 1/2$. Then, by using (1.71) and introducing the light intensity according to (1.55), we obtain

$$R_{\text{abs}}(\omega) = \frac{2\pi}{\hbar} |H_{\text{scat}}(\omega)|^2 \frac{1}{4}\rho_c \frac{1}{\hbar\omega} \frac{e^2\eta_0}{n_r m_c \omega^2}. \tag{1.73}$$

If we introduce the scattering rate inside the band as follows:

$$[\tau_{\text{scat}}(\omega)]^{-1} = \frac{2\pi}{\hbar} |H_{\text{scat}}(\omega)|^2 \frac{1}{4}\rho_c, \tag{1.74}$$

we obtain the rate of change of the two-dimensional energy density in QWs,

$$\frac{dU}{dt} = \hbar\omega N_{\text{2D}} R_{\text{abs}}(\omega) = \frac{e^2\eta_0}{n_r \tau_{\text{scat}}} \frac{N_{\text{2D}} I}{m_c[\omega^2 + \tau_{\text{scat}}^{-2}]} = \alpha_{fc}(\omega) I, \tag{1.75}$$

where we have added the additional term $\tau_{\text{scat}}^{-2}$ into the denominator in order to phenomenologically take into account the "uncertainty" in frequency caused by the scattering, but this can be rigorously derived if one follows full second-order perturbation theory rather than the simple Golden rule. Finally, for the per-well free-carrier absorption we obtain

$$\alpha_{fc}(\omega) = \frac{4\pi\alpha_0}{n_r} \frac{N_{\text{2D}} \hbar \tau_{\text{scat}}^{-1}}{m_c[\omega^2 + \tau_{\text{scat}}^{-2}]}. \tag{1.76}$$

Numerically, the typical scattering time is determined by the interaction with longitudinal-optical (LO) phonons, considered in greater detailed in the Section 1.4, but a typical value of this scattering rate is about $(1/200)$ fs$^{-1}$ for the InGaAs, which for the doping density of $N_{\text{2D}} \sim 5 \times 10^{11}$ cm$^{-2}$ results in free-carrier absorption per QW, as shown in Fig. 1.13. For a waveguide with effective three-dimensional doping density on the scale between $10^{17}$ and $10^{18}$ cm$^{-3}$ the absorption coefficient is between 1 and 10 cm$^{-1}$ depending on the wavelength, which are values that are typically being measured experimentally.

If we neglect the frequency dependence of the scattering time, this expression (1.76) is exactly the one that follows from the Drude expression for the Drude theory for free-carrier complex conductivity:

$$\sigma(\omega) = \frac{e^2 N_{\text{2D}} \tau_{\text{scat}}}{m_c(1 + j\omega\tau_{\text{scat}})}. \tag{1.77}$$
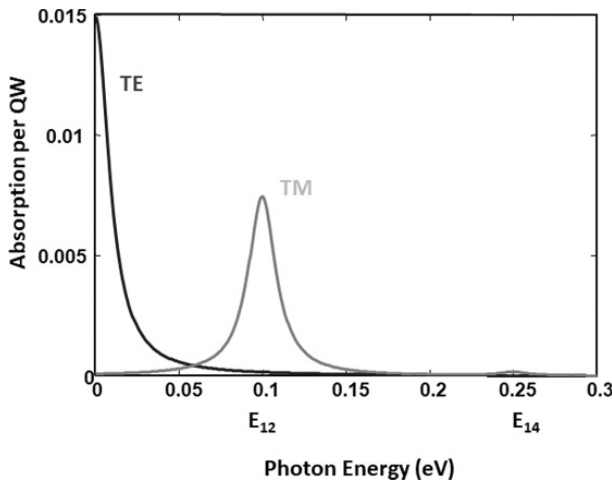
**Fig. 1.13** Spectra of free-carrier (TE) and intersubband (TM) absorption in doped QW. Note that the areas under the curves are equal.

If we now integrate (1.76) over the frequencies, we obtain

$$\int_0^\infty \alpha_{\text{fc}}(\omega)d\omega = \frac{2\pi^2\alpha_0\hbar N_{2\text{D}}}{n_{\text{r}}m_{\text{c}}}. \tag{1.78}$$

Then, if we integrate over the frequencies of the ISB absorption as in (1.68), we obtain

$$\int \alpha_{12}(\omega)d\omega = \frac{4\pi^2\alpha_0}{n_{\text{r}}}\omega_{12}N_{2\text{D}}z_{12}^2. \tag{1.79}$$

Now we can invoke the oscillator sum rule for all ISB transitions originating from the subband 1,

$$\sum_{m=2}^\infty \omega_{1m}z_{1m}^2 = \hbar/2m_{\text{c}}, \tag{1.80}$$

and obtain a very important result:

$$\int_0^\infty \alpha_{\text{fc}}(\omega)d\omega = \int_0^\infty \sum_{m=2}^\infty \alpha_{1m}(\omega)d\omega = \frac{2\pi^2\alpha_0\hbar N_{2\text{D}}}{n_{\text{r}}m_{\text{c}}}. \tag{1.81}$$

This result shows that ISB transitions are nothing but the quantized free-carrier transitions with total oscillator strength (integrated absorption) conserved as it is transferred from the broad-band continuous free-carrier absorption to the discrete ISB transitions. The quantization (one can think of it as reflections from the QW walls) relaxes momentum conservation rules, hence in ISB transitions there is no need for the "recoil" provided by phonon or impurity – the walls do the job perfectly well. Therefore, for a TM wave the free-carrier absorption is absent as long as all the carriers remain in the lowest subband. Of course, in QCLs the carriers can get excited to the

upper subbands from where they do get absorbed into the continuum states [22]. This absorption typically does not have sharp features and sometimes is referred to as free-carrier absorption, but in truth it cannot be described by a simple $\omega^{-2}$ dependence (1.76), hence it is better to refer to it as nonresonant ISB absorption [22].

### 1.2.4 Comparison of the Band-to-Band and ISB Transition Strength

Let us now compare the absorption in a single QW for interband (1.58) and ISB transitions (1.68). If the transition is allowed, then, according to the oscillation sum rule,

$$\omega_{12} z_{12}^2 \approx \hbar/2m_c \tag{1.82}$$

and

$$\alpha_{12}^{\mathrm{TM}}(\omega_{12}) = \frac{2\pi\alpha_0}{n_r} \frac{\hbar^2}{m_c} \frac{N_{2D}}{\Gamma} \frac{N_{QW}}{W_{eff}}. \tag{1.83}$$

Then we obtain for the ratio of ISB absorption (1.83) to the band-to-band absorption [8] (1.58),

$$\frac{\alpha_{12,\parallel}}{\alpha_{hh,\perp}} = \frac{2N_{2D}}{\pi\Gamma} \frac{\pi\hbar^2}{m_c} \approx \frac{2}{\pi} \frac{N_{2D}}{\rho_{cv}\Gamma}. \tag{1.84}$$

This is essentially the relation of effective densities of states for ISB and band-to-band transitions. The oscillator strengths of the transitions are for all practical purposes identical, and the "giant dipole moment" of the ISB transition is simply the consequence of a typical ISB transition having lower energy than a typical band-to-band transition. This can be shown in a more direct way by estimating the dipole moment of the band-to-band transition as follows:

$$z_{cv} \sim P_{cv}\hbar/m_0 E_g \sim \left(\frac{\hbar^2}{2m_c E_g}\right)^{1/2}, \tag{1.85}$$

which for GaAs turns out to be respectable 7Å – much larger than the bond length or even lattice constant. The result does not contradict the Bloch theorem, which only states that the electron wavefunction is periodic with a lattice constant and not that it is confined on the scale of lattice constant. Now we can re-write (1.82) by using the definition of effective mass (1.37) as follows:

$$z_{12} = \sqrt{\frac{\hbar}{2m_c\omega_{12}}} = \sqrt{\frac{P^2\hbar}{m_0^2 E_g \omega_{12}}} = \frac{P\hbar}{m_0 E_g}\sqrt{\frac{E_g}{\hbar\omega_{12}}} = z_{cv}\sqrt{\frac{E_g}{E_{12}}}. \tag{1.86}$$

So, to repeat, the one and only reason why an ISB transition has a relatively large dipole is simply the fact that it occurs typically in the mid- and far-IR where the transition energy is low. If, however, one compares the strength of an ISB transition in GaN and a band-to-band transition in InGaAs for the same wavelength, say 1.55μm, the dipole moments will be essentially identical. Thus, the main advantage of ISB transitions lies not as much in their strength, but in their flexibility – ability to obtain transitions at any mid- or far-IR wavelength by using standard medium-gap material systems like GaAs or InP, rather than venturing to more exotic narrow-gap III-V and II-VI materials.

## 1.3 Intersubband Scattering

Scattering plays an extremely important role in QCLs, as it is an inextricable part of both carrier transport through the QCL as well as of the lasing itself. One should distinguish between intrasubband and intersubband scattering. Intrasubband scattering is responsible for carrier thermalization as well as for level broadening. Intersubband scattering, in addition to contributing to electroluminescence (EL) linewidth broadening and carrier thermalization, is also responsible for the population and depopulation of laser levels, and is thus the key mechanism that determines whether population inversion can actually be attained between the upper and lower laser levels. In general, intrasubband scattering occurs on a significantly shorter time scale than intersubband scattering, mostly due to fact that the interaction strength does not involve the overlap between two different envelope wavefunctions. Therefore, often one can analyze the dynamics of populations in a QCL assuming that within each subband a thermal equilibrium has been reached. At any rate, intrasubband relaxation is just there and cannot be changed significantly by design; hence, we shall not consider it in this short introduction. Intersubband relaxation, on the other hand, depends on the overlap between the envelope wavefunction and the momentum change involved in scattering, hence it can be engineered to achieve favorable relationships between the lifetimes of upper- and lower-laser levels and simultaneously suppress leakage from the upper level, thus improving QCL characteristics.

There are many different mechanisms that contribute to scattering, but clearly, three of them are the dominant ones: scattering by the longitudinal-optical (LO) phonons, interface-roughness (IFR) scattering, and alloy-disorder (AD) scattering. The other important processes – acoustic-phonon scattering and electron-electron scattering – are always present as well, but their influence is not nearly as critical as those of the first three scattering processes.

### 1.3.1 Intersubband Scattering by Longitudinal-Optical Phonons

We start with the longitudinal-optical (LO) phonon scattering because it is this process that largely allows the population inversion to be achieved in QCLs [23]. That is why we shall derive all the relevant expressions rigorously. An LO phonon [24, 25] is an elastic wave propagating in the material with lattice basis consisting of two atoms, such as in zinc-blende lattice. In the optical mode, two basis atoms (cation and anion) move in the opposite directions, as shown in Fig. 1.14(a). Now, since two atoms comprising the basis are actually charged ions with effective charge of $+e^*$ for cation (Ga) and negative charge $-e^*$ for the anion (As), where $e^* = fe$ and a coefficient $0 < f < 1$ describes the polarity of the bond. Thus, if one introduces a relative displacement of the two ions as $\boldsymbol{u} = \boldsymbol{u}_c - \boldsymbol{u}_a$, then one can write the differential equation of motion for the ions in the optical-phonon mode in the presence of an external harmonic electric field:

$$\frac{d^2\boldsymbol{u}}{dt^2} + \omega_{\text{TO}}^2\boldsymbol{u} = \frac{1}{2}\frac{e^*}{M_r}\boldsymbol{E}_0 e^{i(\boldsymbol{q}\cdot\boldsymbol{r}-\omega t)} + c.c., \tag{1.87}$$

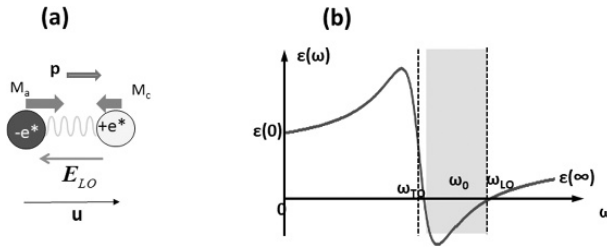where the frequency $\omega_{\text{TO}}$ at small wave vectors $q$ can be found as follows:

**Fig. 1.14** (a) Optical vibrations in a diatomic lattice of III-V semiconductor; (b) dispersion of the dielectric constant of polar semiconductor.

$$\omega_{TO}^2 \approx 2K/M_r, \tag{1.88}$$

where $K$ is the restoring force acting upon the ions and

$$M_r = M_c M_a (M_c + M_a) \tag{1.89}$$

is the reduced mass of the cation and anion. The ion displacement can naturally be written as a harmonic wave $\boldsymbol{u}(\boldsymbol{r}, t) = \boldsymbol{u}_0 e^{i(\boldsymbol{q}\cdot\boldsymbol{r}-\omega t)} + c.c.$ and, due to the presence of ion charge, each bond becomes polarized with a time-dependent dipole moment given by

$$\boldsymbol{p}(\boldsymbol{r}, t) = \frac{1}{2} e^* \boldsymbol{u}_0 e^{i(\boldsymbol{q}\cdot\boldsymbol{r}-\omega_0 t)} + c.c. \tag{1.90}$$

Hence, there exists a polarization wave in the lattice,

$$\boldsymbol{P}_L(\boldsymbol{r}, t) = \frac{1}{2} N e^* \boldsymbol{u}_0 e^{i(\boldsymbol{q}\cdot\boldsymbol{r}-\omega_0 t)} + c.c., \tag{1.91}$$

where $N$ is the density of bonds. The total polarization in the semiconductor must also include the electronic polarization, i.e., the polarization of the electrons inside the valence bonds, described by the electronic susceptibility in the presence of an external electric field

$$\boldsymbol{P}_{el}(\boldsymbol{r}, t) = \frac{1}{2} \varepsilon_0 \chi_{el} \boldsymbol{E}_0 e^{i(\boldsymbol{q}\cdot\boldsymbol{r}-\omega_0 t)} + c.c., \tag{1.92}$$

where the electronic susceptibility $\chi_{el}$ can be considered frequency independent as long as the frequency is far from the absorption edge in the semiconductor; thus it can be designated as

$$\chi_{el} = \varepsilon(\infty) - 1, \tag{1.93}$$

where $\varepsilon(\infty)$ is the dielectric constant in the optical range; i.e., at frequencies much higher than $\omega_{TO}$. Solving (1.87) and using (1.91) we immediately obtain

$$\boldsymbol{P}_L(\boldsymbol{r}, t) = \frac{N(e^*)^2 \boldsymbol{E}_0 e^{j(\boldsymbol{q}\cdot\boldsymbol{r}-\omega_0 t)}}{M_r(\omega_{TO}^2 - \omega^2)} + c.c., \tag{1.94}$$

and the total electric displacement can be found as follows:

$$D(r, t) = \varepsilon_0 E(r, t) + P_L(r, t) + P_{el}(r, t)$$

$$= \frac{1}{2}\varepsilon_0\varepsilon(\infty)E_0 e^{j(q \cdot r - \omega_0 t)} + c.c. + P_L(r, t) = \frac{1}{2}\varepsilon_0\varepsilon(\omega)E_0 e^{j(q \cdot r - \omega_0 t)} + c.c.$$

(1.95)

From (1.94) and (1.95) we immediately obtain the expression for the frequency-dependent dielectric constant,

$$\varepsilon(\omega) = \varepsilon(\infty) + \frac{N(e^*)^2}{\varepsilon_0 M_r(\omega_{TO}^2 - \omega^2 - i\omega\gamma)},$$

(1.96)

where $\gamma$ is the phonon-scattering rate. The dispersion of the real part of dielectric constant is shown in Fig. 1.14(b). Near $\omega = \omega_{TO}$ the dielectric constant becomes very large, indicating that displacement can be not-zero even with a near-zero electric field. This is the resonance frequency of the transverse optical phonon which engenders no electric field. But at a frequency $\omega_{LO}$, defined as

$$\omega_{LO}^2 = \omega_{TO}^2 + \frac{N(e^*)^2}{\varepsilon_0\varepsilon(\infty)M_r},$$

(1.97)

the dielectric constant is zero and that means that a longitudinal wave can propagate at this frequency. Indeed, if we assume that no external electric field is applied and the LO phonon is longitudinal, i.e., $\nabla \cdot u = q \cdot u = qu$, one obtains from the Maxwell equation for the displacement,

$$\nabla \cdot D = \varepsilon_0\varepsilon(\infty)q \cdot E_{LO} + q \cdot P_L = \varepsilon_0\varepsilon(\infty)qE_{LO} + qNe^*u = 0,$$

(1.98)

where the intrinsic field induced by the LO phonon is $E_{LO} = -Ne^*u/\varepsilon_0\varepsilon(\infty)$, now adds the restoring force into the equation of motion (1.87),

$$\frac{d^2u}{dt^2} + \omega_{TO}^2 u = \frac{-N(e^*)^2}{\varepsilon_0\varepsilon(\infty)M_r}u,$$

(1.99)

from which the expression for eigenfrequency (1.97) readily follows. One can also obtain the expression for the dielectric constant at low frequencies from (1.96):

$$\varepsilon(0) = \varepsilon(\infty) + \frac{N(e^*)^2}{\varepsilon_0 M_r\omega_{TO}^2}.$$

(1.100)

From (1.97) and (1.100) one obtains the Lyddane–Sachs–Teller relation [26]:

$$\frac{\omega_{LO}^2}{\omega_{TO}^2} = \frac{\varepsilon(0)}{\varepsilon(\infty)}.$$

(1.101)

Now, also from (1.97), we can find the effective ion charge:

$$e^* = [\varepsilon_0\varepsilon(\infty)M_r\omega_{LO}^2[1 - \varepsilon(\infty)/\varepsilon(0)]/N]^{1/2},$$

(1.102)

and the expression for the electric field:

$$\boldsymbol{E}_{\text{LO}} = -\frac{1}{2q}\sqrt{\frac{NM_{\text{r}}}{\varepsilon'\varepsilon_0}}\omega_{\text{LO}}^2\boldsymbol{u}_0 e^{i(\boldsymbol{q}\cdot\boldsymbol{r}-\omega_{\text{LO}}t)} + c.c., \tag{1.103}$$

where

$$\frac{1}{\varepsilon'} = \frac{1}{\varepsilon(\infty)} - \frac{1}{\varepsilon(0)}. \tag{1.104}$$

For both GaAs and lattice-matched to InP substrate $Ga_{0.47}In_{0.53}As$ $1/\varepsilon' \sim 0.014$. The potential of this electric field produced by LO phonon is then

$$\Phi_{\text{LO}} = \frac{1}{2q}\sqrt{\frac{NM_{\text{r}}}{\varepsilon_0\varepsilon'}}\omega_{\text{LO}}^2 u_0 e^{i(\boldsymbol{q}\cdot\boldsymbol{r}-\omega_{\text{LO}}t)} + c.c. \tag{1.105}$$

The $q$-vector dependence of this scattering potential is of utmost importance to the QCL. As we shall see, it is this dependence that facilitates achieving population inversion. Now, the energy of the LO-phonon mode is $NVM_r\omega_{\text{LO}}^2 u_0^2/2$, where $V$ is the quantization volume that can be quantized in increments of $\hbar\omega_{\text{LO}}$. Hence the ion displacement in the mode with $n_{\text{LO}}$ phonons in it is expressed by

$$NM_{\text{r}}\omega_{\text{LO}}^2 u_0^2/2 = (n_{\text{LO}} + 1/2)\hbar\omega_{\text{LO}}/V, \tag{1.106}$$

where

$$n_{\text{LO}} = \frac{1}{\exp(\hbar\omega_{\text{LO}}/k_{\text{B}}T) - 1}. \tag{1.107}$$

The Hamiltonian of interaction between the phonons and electrons is then given by [27]

$$H_{\text{LO}}^2 = e^2\Phi_{\text{LO}}^2 = \frac{e^2\hbar\omega_{\text{LO}}}{2\varepsilon_0\varepsilon'q^2V}\left(n_{\text{LO}} + \frac{1}{2} \pm \frac{1}{2}\right), \tag{1.108}$$

where the $\pm$ signs correspond to the emission (absorption) of LO phonons. For the most part we are interested in the phonon-emission processes.

Let us now consider LO-phonon-assisted scattering between two subbands, $m$ and $n$, separated by an energy $E_{mn}$, as shown in Fig. 1.15 [28–32]. We assume that the electron resides near the bottom of the upper subband $m$ and its in-plane wavevector $k_{\perp m} \approx 0$. To conserve the energy, the electrons in the final state in subband 2 must all have a kinetic energy as follows:

$$\hbar^2 k_\perp^2/2m_{\text{c}} = E_{mn} - \hbar\omega_{\text{LO}}. \tag{1.109}$$

Now, we can use the Fermi Golden rule to write the expression for the scattering rate as such:

$$R_{\text{LO}m\to n} = \frac{2\pi}{\hbar}\sum_{\boldsymbol{q}} \langle m| H_{\text{LO}}^2 |n\rangle\, \delta(E_{mn} - \hbar\omega_{\text{LO}} - \hbar^2 k_\perp^2/2m_{\text{c}}). \tag{1.110}$$

Next, we go from the summation over the phonon wavevector $\boldsymbol{q}$ to integration and represent this wavevector as the sum of normal and in-plane wavevectors:

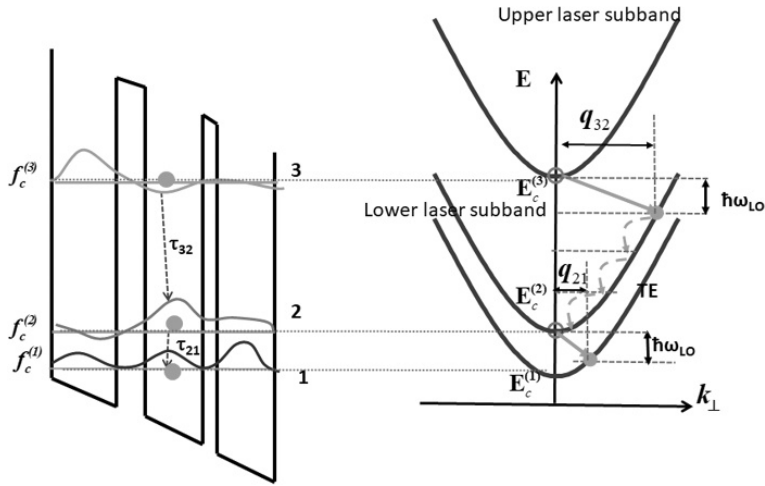$$\boldsymbol{q} = \boldsymbol{q}_z + \boldsymbol{q}_\perp, \tag{1.111}$$

**Fig. 1.15** Energies and in-plane wavevectors involved in LO-phonon scattering in QCLs. Larger in-plane wavevectors are involved in the transition 3→1 than in transition 2→1, which causes the lifetime of level 3 to be longer than that of level 2.

where

$$\boldsymbol{q}_{\perp} \approx \boldsymbol{k}_{\perp}. \tag{1.112}$$

The result is as follows:

$$R_{\text{LO}m\to n} = \frac{1}{8\pi^3}\frac{2\pi}{\hbar}\int\limits_{-\infty}^{\infty}\int\limits_{0}^{\infty}\frac{e^2\hbar\omega_{\text{LO}}}{2\varepsilon_0\varepsilon'\left(q_{\perp}^2+q_z^2\right)}G_{mn}^2(q_z)\frac{2m_{\text{c}}}{\hbar^2}\delta(q_{\perp}^2-q_0^2)\pi\,dq_{\perp}^2\,dq_z\,(n_{\text{LO}}+1)$$

$$= \frac{e^2\omega_{\text{LO}}m_{\text{c}}}{4\pi\varepsilon_0\varepsilon'\hbar^2}\int\limits_{-\infty}^{\infty}\frac{G_{mn}^2(q_z)}{(q_0^2+q_z^2)}dq_z, \tag{1.113}$$

where

$$G_{mn}(q_z) = \int f_{\text{c}}^{(m)}(z)e^{iq_z z}f_{\text{c}}^{(n)}(z)dz \tag{1.114}$$

and

$$q_{mn}^2 = \frac{2m_{\text{c}}}{\hbar^2}(E_{mn}-\hbar\omega_{\text{LO}}). \tag{1.115}$$

The double integral in (1.113) can be evaluated as

$$\int\limits_{-\infty}^{\infty}\frac{e^{iq_z(z_1-z_2)}}{q_z^2+q_{mn}^2}dq_z = \pi\exp(-q_{mn}|z_1-z_2|)/q_{mn}, \tag{1.116}$$

and one finally obtains the expression

$$R_{\text{LO}m\to n} = \frac{e^2\omega_{\text{LO}}m_{\text{c}}}{4\varepsilon_0\varepsilon'\hbar^2}\frac{F_{mn}(q_{mn})}{q_{mn}}, \tag{1.117}$$

where

$$F_{mn}(q_{mn}) = \int \int f_c^{(m)}(z_1) f_c^{(n)}(z_1) \exp(-q_{mn}|z_1 - z_2|) f_c^{(m)}(z_2) f_c^{(n)}(z_2) dz_1 dz_2. \quad (1.118)$$

Let us introduce

$$q_0 = \sqrt{\frac{2m_c \omega_{LO}}{\hbar}}. \quad (1.119)$$

For GaAs $q_0 \sim 0.25\,\text{nm}^{-1}$ while for $\text{Ga}_{0.47}\text{In}_{0.53}\text{As}$ $q_0 \sim 0.25\,\text{nm}^{-1}$, and normalizing the wavevector $q$ as $Q_{mn} = q_{mn}/q_0 = \sqrt{E_{mn}/\hbar\omega_{LO} - 1}$ and the coordinate $z$ as $Z = zq_0$, we obtain

$$R_{\text{LO}m \to n} = \frac{e^2 q_0}{8\varepsilon_0 \varepsilon' \hbar} F_{mn}(Q_{mn}) = \frac{\pi}{2\varepsilon'} \alpha_0 c q_0 F_{mn}(Q_{mn}), \quad (1.120)$$

where $\alpha_0$ is the fine structure constant and

$$F_{mn}(Q_{mn}) = Q_{12}^{-1} \int \int f_c^{(m)}(Z_1) f_c^{(n)}(Z_1) \exp(-Q_{mn}|Z_1 - Z_2|) f_c^{(m)}(Z_2) f_c^{(n)}(z_2) dZ_1 dZ_2. \quad (1.121)$$

The term in front of the $F_{mn}(Q_{mn})$ in (1.120) for GaAs is $1.2 \times 10^{13}\,s^{-1}$, while for $\text{Ga}_{0.47}\text{In}_{0.53}\text{As}$ it is $0.9 \times 10^{13}\,s^{-1}$. What is left to calculate is $F_{12}(Q_{12})$. To do it, we consider an example of a square QW with infinitely high walls, having envelope wavefunctions:

$$f_c^{(m)}(Z) = \sqrt{\frac{2}{aq_0}} \sin(m\pi Z/aq_0), \quad (1.122)$$

where $a$ is the QW width. The results are shown in Fig. 1.16(a) for the allowed transitions in the QW with the width ranging from 5 to 20 nm. Of course, the sideband separation $E_{mn}$ cannot be easily varied for a given well thickness, and the actual shape of QCL's active regions is quite different from the square QW, but the general trend shown in Fig. 1.16(a) is correct, as the ISB scattering becomes strongest right when the ISB is resonant with the phonon energy and can lead to lifetimes as short as 200–250 fs. At the same time when the transition energy is in the range of 120–250 meV (which is the case for lasing transitions in the mid-IR), the scattering strength is reduced and lifetimes approach 1 ps. Using this fact one can achieve the difference between relaxation rates, $R_{\text{LO}3 \to 2}$ and $R_{\text{LO}2 \to 1}$, in Fig. 1.15, and make sure that the condition $\tau_{32} > \tau_{21}$ necessary for achieving population inversion in QCL is satisfied. One can further reduce the LO-scattering rates by considering transitions with reduced oscillator strength. For instance, as shown in Fig. 1.16(b), the ISB LO scattering for the dipole-forbidden transition $R_{\text{LO}3 \to 1}$ is substantially weaker than for dipole-allowed transition $R_{\text{LO}2 \to 1}$. This method is used for the case when the transition energy is small, such as in the THz region [33, 34]. But of course, the increase in lifetime is accompanied by a reduction in gain in this case, which makes attainment of the laser threshold in the THz range more difficult.
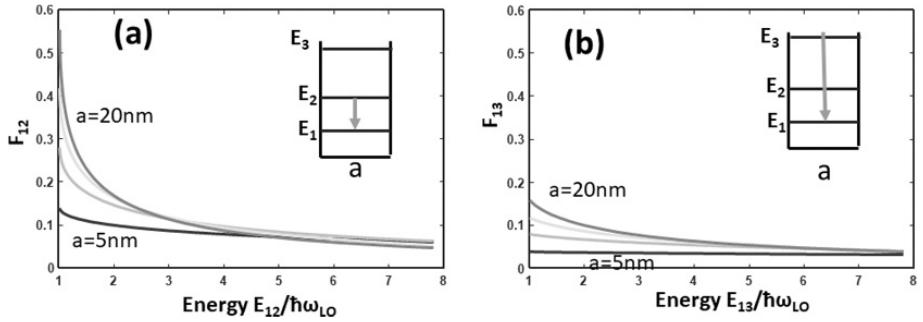
**Fig. 1.16** Relative strength of intersubband LO-phonon scattering vs. the intersubband separation energy for: (a) dipole-allowed and (b) dipole-forbidden transitions.

### 1.3.2 Alloy-Disorder Scattering

The active region of a QCL consists of a large number of wells and barriers having different compositions which can be binary, ternary, and sometimes quaternary alloys. The alloy scattering occurs in the ternary and quaternary materials such as InGaAs, InAlAs, or InGaAsP [31, 32, 35–38]. Consider a simple model with coupled QWs as shown in Fig. 1.17(a) [27]. At least one, and more often both QW and barrier materials are at least ternary or sometimes quaternary alloys. We consider a most simple well material, $In_xGa_{1-x}As$, that is often used in mid-IR QCLs. In Fig. 1.17(b) we show the arrangement of cation atoms In or Ga in the cation plane – and this arrangement is clearly aperiodic. Since the states in the conduction band are most strongly associated with S-states of cations, these electrons will see different effective potential near In and Ga ions – we should refer to them for generality as (A) and (B) ions – because In (A) and Ga (B) have different bandgaps and electron affinities. Let us now introduce the aperiodic lattice potential $U_{lat}(\boldsymbol{r})$, shown in Fig. 1.17(c), which has a constant value $E_{A(B)}$ within the distance $r_0$, commensurate with the size of the unit cell, from the cation A(B). This aperiodic potential differs from the mean lattice potential $\langle U_{lat}\rangle (\boldsymbol{r})$, which is periodic with value of $\bar{E} = xE_A + (1-x)E_B$ at each unit cell, as shown by the dashed line in Fig. 1.17(c). The alloy-scattering potential is then simply the difference between the local and average lattice potentials seen by the conduction electron [12, 27]; i.e.,

$$\delta U(\boldsymbol{r}) = \begin{cases} \delta E_A = E_A - \bar{E} = (1-x)(E_A - E_B) = (1-x)\delta E_{AB} & \text{on A site,} \\ \delta E_B = E_A - \bar{E} = x(E_B - E_A) = -x\delta E_{AB} & \text{on B site,} \end{cases}$$

(1.123)

where $\delta E_{AB} = E_A - E_B$ as shown in Fig. 1.17(d).

We can now calculate the matrix element of the alloy perturbation, at one particular A(B) site with co-ordinate $\boldsymbol{r}_l$, between a given state in the subband $m$ of in-plane wavevector $\boldsymbol{k}_{\perp m}$ and one in the subband $n$ of wavevector $\boldsymbol{k}_{\perp n}$, as shown in Fig. 1.18:
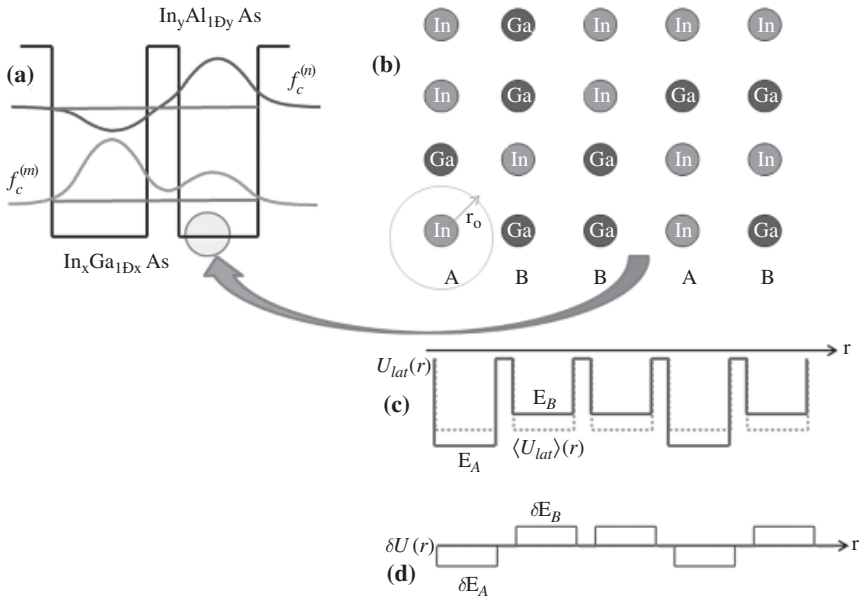
**Fig. 1.17** (a) Electron states in the QW comprising alloys. (b) Aperiodic arrangement of cations in an alloy. (c) Aperiodic lattice potential $U_{lat}(\mathbf{r})$ and its average value $< U_{lat}>(\mathbf{r})$. (d) Alloyed perturbation potential $\delta U_{lat}(\mathbf{r})$.

$$\langle m| \, \delta U(z_l) \, |n\rangle = S^{-1} \int\limits_{|r-r_l|<r_0} \delta E_{A(B)} f_c^{(m)}(z) f_c^{(n)}(z) e^{i(k_{\perp m}-k_{\perp n})\cdot r_\perp} d\mathbf{r}_\perp dz$$
$$\approx V_0 S^{-1} \delta E_{A(B)} f_c^{(m)}(z_l) f_c^{(n)}(z_l), \qquad (1.124)$$

where $V_0 = \frac{4}{3}\pi r_0^3$, $S$ is the quantization area in the plane of QWs, and we have made the reasonable assumptions that $k_{\perp m,n} << 1/r_0$ and that the envelope wavefunctions do not change much over one unit cell – hence the AD scattering does not depend on the wavevector – which is dramatically different from the LO-phonon scattering process of Fig. 1.15. Therefore, the alloy-scattering due to one particular lattice site $l$ can be found with a Fermi Golden rule as follows:

$$R_{mn}^{A(B)}(z_l) = \frac{2\pi}{\hbar} V_0^2 S^{-1} \left|\delta E_{A(B)}\right|^2 \left|f_c^{(m)}(z_l) f_c^{(n)}(z_l)\right|^2 \rho_c, \qquad (1.125)$$

where $\rho_c = m_c/2\pi\hbar^2$ is the density of states for one spin.

Now we need to perform the summation over all the lattice sites within a region occupied by an alloy – in our example a QW or a barrier region defined as $z_1 < z < z_2$. The volume of a unit cell in f.c.c. lattice is $a_0^3/4$; therefore the density of A atoms is $N_A = 4x/a_0^3$ and the density of B atoms is $N_B = 4(1-x)/a_0^3$. Therefore, performing integration over these densities, we obtain
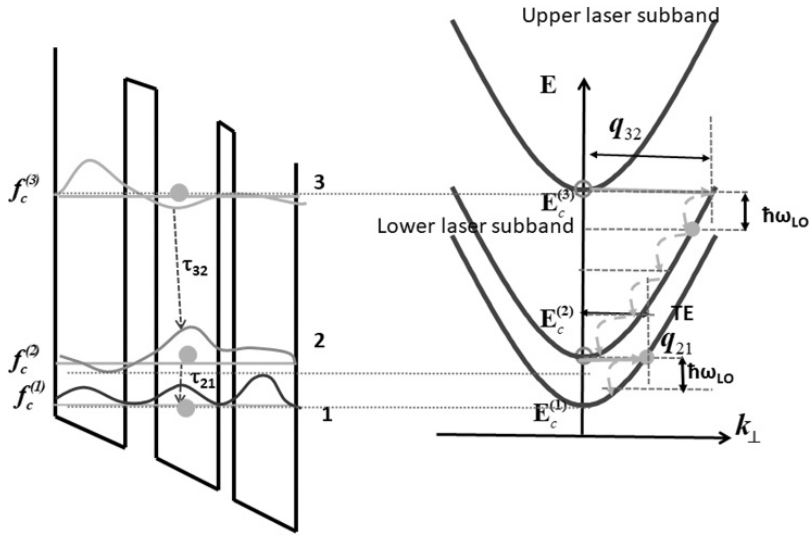
**Fig. 1.18** Energies and in-plane wavevectors involved in elastic intersubband scattering: alloy disorder, interface roughness, or ionized impurity.

$$R_{AD,m \to n} = \int\limits_{S} \int\limits_{z_1}^{z_2} N_A R_{mn}^A(z_l) dz_l d\boldsymbol{r}_\perp + \int\limits_{S} \int\limits_{z_1}^{z_2} N_B R_{mn}^B(z_l) dz_l d\boldsymbol{r}_\perp$$

$$= \frac{64\pi^3 r_0^6}{9\hbar a_0^3} (\delta E_{AB})^2 x(1-x) \int\limits_{z_1}^{z_2} \left| f_c^{(m)}(z_l) f_c^{(n)}(z_l) \right|^2 dz_l \rho_c. \tag{1.126}$$

The size of $r_0$ is taken as half of the separation from the next cation in the f.c.c. lattice, i.e., $r_0 = a_0/2\sqrt{2}$, hence:

$$R_{AD,m \to n} = \frac{\pi^2 a_0^3 m_c}{72\hbar^3} (\delta E_{AB})^2 x(1-x) \int\limits_{z_1}^{z_2} \left| f_c^{(m)}(z_l) f_c^{(n)}(z_l) \right|^2 dz_l. \tag{1.127}$$

Let us consider an example of a $Ga_{0.47}In_{0.53}$ As with $\delta E_{AB} \sim 0.6\,\text{eV}$– the term outside the integral is equal to $0.82 \times 10^{13}\,\text{nm}^{-1}\,\text{s}^{-1}$ and the wavefunctions under the integral can be normalized to the QW width as $Z = z_l/a$ so that

$$R_{AD,m \to n} \sim \frac{0.82 \times 10^{13}}{a} F_{AD}\,\text{s}^{-1}, \tag{1.128}$$

where the QW width $a$ is in nanometers, and $F_{AD} = \int_{Z_1}^{Z_2} \left| f_c^{(m)}(Z) f_c^{(n)}(Z) \right|^2 dZ < 1$ is the dimensionless overlap between the electron densities of the two states in the alloy region. Therefore, for a 20 nm active region the alloy-scattering time can be a few picoseconds, which is typically longer than LO-phonon scattering, but definitely cannot be neglected. Furthermore, the upper laser states are located, while using high conduction-band offset ternary materials where the lower states are located,

on the one hand, the upper-state lifetime is enhanced due to reduced alloy-disorder scattering, and, on the other hand, the lower-state lifetime is decreased due to enhanced interface-roughness scattering (see 1.3.3). Thus, one can significantly improve the key lasing parameter – the lifetime ratio $\tau_{32}/\tau_{21}$, as shown in [35]. Of course, in THz QCLs with reduced LO-phonon scattering, the influence of the alloy scattering is even more pronounced. It should also be noted that the numerical factor in the result (1.127) strongly depends on the choice of the effective distance $r_0$ over which alloy disorder is "felt" by the electrons hence it should not be treated as an "exact" result. Note that [32, 37, 39] use a different approach that treats alloy scattering as a special case of interface-roughness scattering and obtain a result that differs from (1.127) by only approximately 10%. No matter what model is assumed, however, this order-of-magnitude estimate shows that alloy-disorder scattering is very important [35].

### 1.3.3    Interface-Roughness (IFR) Scattering

Consider another mechanism of ISB elastic scattering – due to the interface roughness [32, 36, 37, 40–42]. As shown in Fig. 1.19(a), the interface between QW and barrier is not smooth but changes as a function of the in-plane coordinate $r = (x, y)$. The interface profile of the $i$th interface can be described as a random function $z_i(r)$ of Fig. 1.19(b), which nevertheless can be characterized by the average position of the interface, $\bar{z}_i$ and a correlation function

$$C(r_1) = \int [z_i(r) - \bar{z}_i] [z_i(r - r_1) - \bar{z}_i] \, dr = \Delta_i^2 e^{-r_1^2/\Lambda^2}, \qquad (1.129)$$
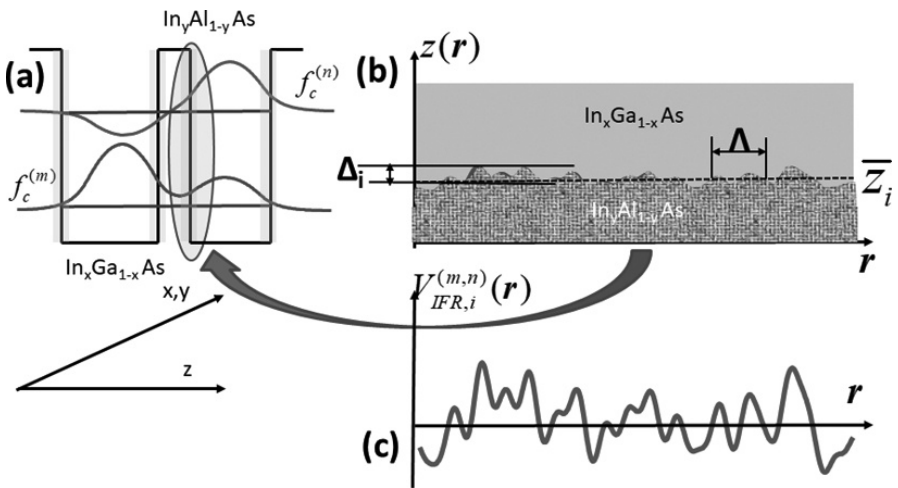


**Fig. 1.19** (a) Electron states in the QW with interface roughness. (b) Interface with roughness. (c) Interface roughness potential $V_{\text{IFR},i}^{(m,n)}$.

where $\Delta_i = \langle (z_i - \bar{z}_i)^2 \rangle^{1/2}$ is the root-mean-square height and $\Lambda$ is the in-plane correlation length.

The perturbation Hamiltonian due to the $i$th interface roughness can be estimated as

$$V_{\text{IFR},i}^{(m,n)}(\boldsymbol{r}) = \Delta E_{\text{c},i} f_{\text{c}}^{(m)}(\bar{z}_i) f_{\text{c}}^{(n)}(\bar{z}_i) [z_i(\boldsymbol{r}) - \bar{z}_i], \qquad (1.130)$$

where $\Delta E_{\text{c},i}$ is the conduction band offset at the $i$th interface. Now, the matrix element for the transition between two states in the conduction band – one near the bottom of the band $m$ with $k_{\perp m} \approx 0$ and the other in the band $n$ with the same energy and the in-plane wavevector $k_\perp \sim \sqrt{2m_{\text{c}}E_{mn}/\hbar^2}$ can be evaluated as

$$V_{\text{IFR}}^{(mn)}(k_\perp) = \sum_i \int V_{\text{IFR},i}^{(mn)}(\boldsymbol{r}) e^{i\boldsymbol{k}_\perp \cdot \boldsymbol{r}} d\boldsymbol{r} = \sum_i \Delta E_{c,i} f_{\text{c}}^{(m)}(\bar{z}_i) f_{\text{c}}^{(n)}(\bar{z}_i) \int [z_i(\boldsymbol{r}) - \bar{z}_i] e^{i\boldsymbol{k}_\perp \cdot \boldsymbol{r}} d\boldsymbol{r},$$
$$(1.131)$$

which is essentially a Fourier transform of the random function $z_i(\boldsymbol{r}) - \bar{z}$. Using the Wiener–Khinchin relation between the correlation function (1.129) and power spectrum of the function, we then obtain

$$\left| V_{\text{IFR}}^{(mn)}(k_\perp) \right|^2 = \sum_i \Delta_i^2 \Delta E_{\text{c},i}^2 \left| f_{\text{c}}^{(m)}(\bar{z}_i) f_{\text{c}}^{(n)}(\bar{z}_i) \right|^2 \times \pi \Lambda^2 e^{-\Lambda^2 k_\perp^2/4}. \qquad (1.132)$$

Assuming that the band offsets, in-plane correlation lengths, and root-mean-square heights are the same for each interface, the IFR scattering rate then can be found [43] using

$$R_{\text{IFR},m \to n} = \frac{\pi m_{\text{c}}}{\hbar^3} \Delta E_{\text{c}}^2 \Delta_i^2 \Lambda^2 F_{\text{IFR}} e^{-\Lambda^2 k_\perp^2/4}, \qquad (1.133)$$

where $F_{\text{IFR}} = \sum_i |f_{\text{c}}^{(m)}(\bar{z}_i) f_{\text{c}}^{(n)}(\bar{z}_i)|^2 < N_i/a^2$, $N_i$ is the total number of interfaces, and $a$ is the extent of the active region. Using $k_\perp \sim \sqrt{2m_{\text{c}}E_{mn}/\hbar^2}$ one can obtain an order-of-magnitude estimate of the maximum possible IFR scattering rate as follows:

$$R_{\text{IFR},m \to n} = \pi N_i \frac{\Delta E_{\text{c}}^2}{\hbar E_{mn}} \frac{\Delta_i^2}{a^2} G_{\text{IFR}}(-\Lambda k_\perp/2), \qquad (1.134)$$

where $G_{\text{IFR}}(x) = 4x^2 \exp(-x^2)$ is the wavefunction whose maximum value of 1.47 is achieved for $x = 1$, i.e., for $\Lambda = \sqrt{2\hbar^2/m_{\text{c}}E_{mn}}$, which is on the scale of a few nanometers. Typical values of correlation length $\Lambda$ reported in literature are indeed about 5–10 nm, while for mean value of $\Delta_i$ it is 0.1–0.15 nm. Therefore, for $N_i = 6$, $a = 15$ nm, $E_{mn} \sim 250$ meV, and $\Delta E_c = 500$ meV one can obtain transitions rates due to IFR as large as $3 \times 10^{12}$ s$^{-1}$. Note that the presence of the energy $E_{mn}$ in the denominator of (1.134) indicates that one can shorten the scattering time $\tau_{21}$ to accelerate the depopulation of the lower laser level in Fig. 1.18. In Fig. 1.20 the values of $G_{IFR}$ are plotted as a function of intersubband energy $E_{mn}$ for three different values of correlation length $\Lambda$. As one can see, for the larger values of $\Lambda$ IFR scattering is larger for the lower values of energy, i.e., it leads to the favorable result $\tau_{21}, \tau_{32}$, but for smaller $\Lambda$ value the situation can be reversed. The best way to engineer the lifetimes is
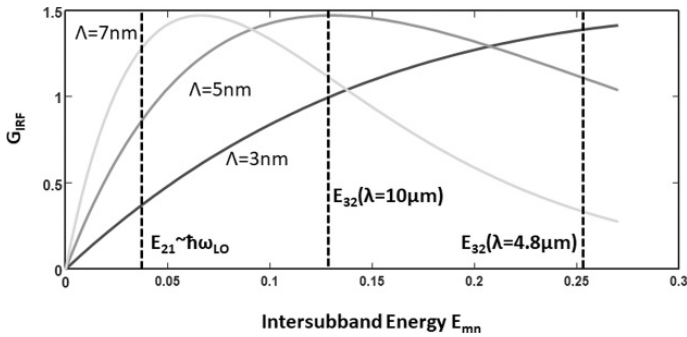
**Fig. 1.20** Interface-roughness scattering dependence on the ISB-transition energy.

to strategically place the interfaces where the two wavefunctions involved in the transitions are large which, in turn, makes $F_{IFR}$ large. Examples of this IFR engineering of nonradiative times can be found in [35, 43] where the lower-level lifetime $\tau_{21}$ was been reduced to less than 0.1 ps without affecting the upper-laser lifetime.

In addition to influencing the lifetimes, IFR also affects the linewidth of the laser transition since both the upper and lower levels are broadened due to intersubband and intrasubband transitions [32, 41, 42]. The intrasubband broadening can be evaluated, for vertical-transition devices, using essentially the same way as the intersubband scattering rate in (1.133), as discussed in [42, 44]:

$$\Delta\omega_{\text{IFR},m\to n} = \frac{\pi m_c}{\hbar^3}\Delta E_c^2 \Delta_i^2 \Lambda^2 \sum_i \left(\left|f_c^{(m)}(\bar{z}_i)\right|^2 - \left|f_c^{(n)}(\bar{z}_i)\right|^2\right)^2 e^{-\Lambda^2 k_\perp^2/4}. \quad (1.135)$$

It should be noted that the in-plane wavevectors $k_\perp$ involved in the optical transitions are small, so the exponential term in (1.135) is close to unity and can be neglected. Furthermore, in most mid-IR QCL designs the electron injection from the reservoir into the active region occurs by tunneling [6] and thus can be strongly affected by IFR scattering [44]. Once the IFR scattering is taken into account, the barrier thickness needs to be reduced to obtain optimal performance, as has been proven in [45] where over 50% wall-plug efficiency has been attained at a heatsink temperature of 77 K. It is therefore quite reasonable to conclude that IFR broadening can easily be as important as that due to LO phonons as shown in [44]. One should also notice that intraband IFR scattering can be dealt with in entirely different fashion by treating it as time-independent localization in real space, i.e., as inhomogeneous broadening [46], still getting the same results in terms of its impact on the linewidth broadening.

### 1.3.4 Other Scattering Processes

The other ISB-scattering processes that can affect the intersubband lifetimes are acoustic phonons scattering (including piezoelectric) [24, 25, 27], and ionized-impurity scattering [47]. But neither one of these processes can be easily engineered to design active regions with favorable arrangement of lifetimes $\tau_{32}, \tau_{21}$. The relatively low doping density of the active regions of less than $10^{17}$ cm$^{-3}$ makes scattering

rates due to ionized donor scattering less than $10^{11}\,\mathrm{s^{-1}}$, and since unlike IFR and AD scattering Coulomb forces are long-ranged, the selective doping of certain wells and barriers does not affect the rates strongly [48, 49] with the notable exception of THz QCLs [33] where the doping is all in the active region. And unlike LO-phonon scattering, the acoustic-phonon Hamiltonian is not wavevector dependent, hence the acoustic scattering rates for the upper- and lower-laser levels are roughly equal and can only be changed by reducing the overlap between the upper- and lower-state wavefunctions (so-called "diagonal transitions"), which is a strategy that can be used for any scattering mechanism and usually leads to reduced transitions' strength and gain.

## 1.4    Conclusions

While far from being a complete description of all the fundamental processes involved in the operation of QCLs, this introductory chapter attempts to answer a few important questions: what is the origin of strong optical intersubband transitions, how does their strength depend on the physical properties of semiconductors and geometry, and how can one reach population inversion enabling QCL operation? This information should help the reader to follow the subsequent chapters of this book. For deeper understanding one should turn attention to a number of excellent books on QCLs [6] and the physics of intersubband transitions [7, 11, 50] in general.

 Nevertheless, a short summary of the most important points made in this chapter can be made, specifically:

- ISB transitions have precisely the same origin as interband transitions, namely, on the microscopic level, the former and latter are both the transitions between the bonding and anti-bonding covalent orbitals in III-V compounds. The strength of ISB transitions is large not due to their unique character, but entirely due to the long wavelengths of the mid-IR or THz radiation.
- The main advantage of ISB transitions is that they can be engineered almost at will (in terms of transition energy and oscillator strength) entirely by changing the geometry of QWs using the same limited and well-tried set of III-V materials, arsenides and phosphides (with the recent addition of nitrides).
- The ISB absorption can also be treated as quantized free-carrier absorption with total oscillator strength of ISB and free-carrier absorption conserved.
- LO-phonon scattering plays the key role in the dynamics of QCLs. Due to fortuitous dependence of ISB LO-scattering rates on the subband energies separation, in the case of mid-IR QCLs, it is precisely the process that makes population inversion possible by assuring that the lower laser level gets depopulated faster than the upper level. This is difficult to attain in THz QCLs where the upper and lower levels are closely spaced and more ingenious methods must be used, as shown in following chapters.
- Interface-roughness and alloy-disorder scattering are both essential to engineering the lifetimes of the energy levels of QCL as well as to tunneling rates,

luminescence linewidth, and injection efficiency, as discussed in detail in Chapter 2.

With these basics placed at the readers' disposal, all I have left is to direct them to the exciting subsequent chapters of this book dealing with more practical aspects of QCLs.

## References

[1] L. C. West and S. J. Eglash, "First observation of an extremely large-dipole infrared transition within the conduction band of a GaAs quantum well," *Appl. Phys. Lett.*, vol. 46, no. 12, pp. 1156–1158, 1985.

[2] B. F. Levine, R. J. Malik, J. Walker, K. K. Choi, C. G. Bethea, D. A. Kleinman, and J. M. Vandenberg, "Strong 8.2 μm infrared intersubband absorption in doped GaAs/AlAs quantum well waveguides". *Appl. Phys. Lett.*, vol. 50, no. 5, pp. 273–275, 1987.

[3] B. F. Levine, K. K. Choi, C. G. Bethea, J. Walker, and R. J. Malik, "New 10 μm infrared detector using intersubband absorption in resonant tunneling GaAlAs superlattices," *Appl. Phys. Lett.*, vol. 50, no. 16, pp. 1092–1094, 1987.

[4] M. Helm, P. England, E. Colas, F. DeRosa, and S. J. Allen, Jr. "Intersubband emission from semiconductor superlattices excited by sequential resonant tunneling," *Phys. Rev. Lett.*, vol. 63, no. 1, pp. 74–77, 1989.

[5] J. Faist, F. Capasso, D. L. Sivco, C. Sirtori, A. L. Hutchinson and A. Y. Cho, "Quantum cascade laser," *Science*, vol. 264, no. 5158, pp. 553–556, 1994.

[6] J. Faist, *Quantum Cascade Lasers*. Oxford: Oxford University Press, 2013.

[7] M. Razeghi, *Technology of Quantum Devices*. London; New York: Springer, 2010.

[8] J. Khurgin, "Comparative analysis of the intersubband versus band-to-band transitions in quantum wells," *Appl. Phys. Lett.*, vol. 62, no. 12, pp. 1390–1392, 1993.

[9] C-H, Lin, R. Q. Yang, D. Zhang, S. J. Murry, S. S. Pei, A. A. Allerman, and S. R. Kurtz, "Type-II interband quantum cascade laser at 3.8 μm," *Electron. Lett.*, vol 33, no.7, pp. 598–599, 1997.

[10] I. Vurgaftmanm, R. Weih, M. Kamp, J. R. Meyer, C. L. Canedy, C S. Kim, M. Kim, W. W. Bewley, C. D. Merritt, and J. Abell, "Interband cascade lasers," *J. Phys. D*: *Appl. Phys.*, vol. 48, no.12, 123001, 2015.

[11] R. Paiella, *Intersubband Transitions in Quantum Structures*. New York: McGraw-Hill, 2006.

[12] G. Bastard, *Wave Mechanics Applied to Semiconductor Heterostructures*. Les Editions de Physique; Les Ulis Cedex, France, New York, NY: Halsted Press, 1988.

[13] P. Bhattacharya, *Properties of III-V Quantum Wells and Superlattices*. London: The Institution of Engineering and Technology, 2007.

[14] E. L. Ivchenko, and G. E. Pikus, *Superlattices and Other Heterostructures: Symmetry and Optical Phenomena*. 2nd ed. Berlin; New York: Springer: Berlin, 1997.

[15] W. A. Harrison, *Solid State Theory*. New York: Dover Publications, 1979.

[16] P. Y. Yu and M. Cardona, *Fundamentals of Semiconductors: Physics and Materials Properties*. 4th ed. Berlin; New York: Springer, 2010.

[17] E. O. Kane, "Band structure of indium antimonide," *J. Phys. Chem. Solids*, vol. 1, no. 4, pp. 249–261, 1957

[18] G. L. Bir, G. E Pikus, *Symmetry and Strain-induced Effects in Semiconductors*. New York: Wiley, 1974.

[19] I. Vurgaftman, J. R. Meyer, and L. R. Ram-Mohan, "Band parameters for III–V compound semiconductors and their alloys," *J. Appl. Phys.*, vol. 89, no. 11, pp. 5815–5875, 2001.

[20] R. Q. Yang, J. M. Xu, and M. Sweeny, "Selection rules of intersubband transitions in conduction-band quantum wells," *Phys. Rev. B*, vol. 50, no.11, pp. 7474–7482, 1994,

[21] J. B. Khurgin, "Intersubband spin pump," *Appl. Phys. Lett.*, vol. 88, no. 12, 123511, 2006.

[22] A. Wittmann, T. Gresch, E. Gini, L. Hvozdara, N. Hoyler, M. Giovannini, and J. Faist, "High-performance bound-to-continuum quantum-cascade lasers for broad-gain applications," *IEEE J. Quantum Electron.*, vol. 44, no. 1, pp. 36–40, 2008.

[23] G. Sun and J. B Khurgin, "Optically pumped four-level infrared laser based on intersubband transitions in multiple quantum wells: feasibility study," *IEEE J. Quantum Electron*, vol. 29, no. 4, pp. 1104–1111, 1993.

[24] B. K. Ridley, *Electrons and Phonons in Semiconductor Multilayers*. 2nd ed.; Cambridge: Cambridge University Press, 2009.

[25] B. K. Ridley, *Quantum Processes in Semiconductors*. 5th ed.; Oxford: Oxford University Press, 2013.

[26] C. Kittel, *Introduction to Solid State Physics*. 8th ed.; Hoboken, NJ: Wiley, 2005.

[27] J. Singh, *Physics of Semiconductors and Their Heterostructures*. New York: McGraw-Hill, 1993.

[28] U. Bockelmann and G. Bastard, "Phonon scattering and energy relaxation in two-, one-, and zero-dimensional electron gases," *Phys. Rev. B*, vol. 42, no. 14, pp. 8947–8951, 1990.

[29] F. Chevoir and B. Vinter, "Calculation of phonon-assisted tunneling and valley current in a double-barrier diode," *Appl. Phys. Lett.*, vol. 55, no. 18, 1859–1861, 1989.

[30] J. Faist, C. Sirtori, F. Capasso, L. Pfeiffer, and K. W. West, "Phonon limited intersubband lifetimes and linewidths in a two-dimensional electron gas," *Appl. Phys. Lett.*, vol. 64, no.7, pp. 872–874, 1994.

[31] Y. Chen, N. Regnault, R. Ferreira, B. F. Zhu, and G. Bastard, "Optical phonon scattering in quantum cascade laser in a magnetic field," *Physics of Semiconductors, AIP Conf, Proc.* vol. 1199, pp. 221–222, 2009.

[32] T. Unuma, M. Yoshita, T. Noda, H. Sakaki, and H. Akiyama, "Intersubband absorption linewidth in GaAs quantum wells due to scattering by interface roughness, phonons, alloy disorder, and impurities," *J. Appl. Phys.*, vol. 93, no. 3, pp. 1586–1597, 2003.

[33] B. S. Williams, H. Callebaut, S. Kumar, and Q. Hu, "3.4-THz quantum cascade laser based on longitudinal-optical-phonon scattering for depopulation," *Appl. Phys. Lett.*, vol. 82, no. 7, pp. 1015–1017, 2003.

[34] Q. Hu, B. S. Williams, S. Kumar, H. Callebaut, and J. L. Reno, "Terahertz quantum cascade lasers based on resonant phonon scattering for depopulation," *Philos. Trans. Roy. Soc. A*, vol. 362, no. 1815, pp. 233–247, 2004.

[35] D. Botez, J. D. Kirch, C. Boyle, K. M. Oresick, C. Sigler, H. Kim, B. B. Knipfer, J. H. Ryu, D. Lindberg III, T. Earles, L. J. Mawst, and Y. V. Flores, "High-efficiency, high-power mid-infrared quantum cascade lasers," *Opt. Mater. Express*, vol. 8, no. 5, pp. 1378–1398, 2018; Erratum: vol. 11, no. 7, p. 1970, 2021.

[36] F. Chevoir and B. Vinter, "Scattering-assisted tunneling in double-barrier diodes: Scattering rates and valley current," *Phys. Rev. B*, vol. 47, no. 12, pp. 7260–7274, 1993.

[37] T. Unuma M. Yoshita, T. Noda, H. Sakaki M. Baba and H. Akiyama, "Sensitivity of intersubband absorption linewidth and transport mobility to interface roughness scattering in GaAs quantum wells," Inst. Phys. Conf. Ser. No 174 (*Proc. of 29th Int. Symp. on Comp. Semicond.*), pp. 379–383, 2003.

[38] A . Vasanelli, A. Leuliet, C. Sirtori, A. Wade, G. Fedorov, D. Smirnov, G. Bastard, B. Vinter, M. Giovannini, and J. Faist, "Role of elastic scattering mechanisms in GaInAs/AlInAs quantum cascade lasers," *Appl. Phys. Lett.*, vol. 89, no. 17, 172120, 2006.

[39] R. Terazzi, "Transport in quantum cascade lasers," Ph.D. dissertation, ETH Zurich, pp. 103–106, 2011.

[40] A. Leuliet, A. Vasanelli, A. Wade, G. Fedorov, D. Smirnov, G. Bastard, and C. Sirtori, "Electron scattering spectroscopy by a high magnetic field in quantum cascade lasers," *Phys. Rev. B*, vol. 73, no. 8, 085311, 2006.

[41] S. Tsujino, A. Borak, E. Müller, M. Scheinert, C. V. Falub, H. Sigg, and D. Grützmacher, "Interface-roughness-induced broadening of intersubband electroluminescence in *p*-SiGe and *n*-GaInAs/AlInAs quantum-cascade structure," *Appl. Phys. Lett.*, vol. 86, no. 6, 062113, 2005.

[42] A. Wittmann, Y. Bonetti, J. Faist, E. Gini, and M. Giovannini, "Intersubband linewidths in quantum cascade laser designs," *Appl. Phys. Lett.*, vol. 93, no. 14, 141103, 2008.

[43] Y. T. Chiu, Y. Dikmelik, P. Q. Liu, N. L. Aung, J. B. Khurgin, and C. F. Gmachl, "Importance of interface roughness induced intersubband scattering in mid-infrared quantum cascade lasers," *Appl. Phys. Lett.*, vol. 101, no. 17, 171117, 2012.

[44] J. B. Khurgin, Y. Dikmelik, P. Q. Liu, A. J. Hoffman, M. D. Escarra, K. J. Franz, and C. F. Gmachl, "Role of interface roughness in the transport and lasing characteristics of quantum-cascade lasers," *Appl. Phys. Lett.*, vol. 94, no. 9, 091101, 2009.

[45] P. Q. Liu, A. J. Hoffman, M. D. Escarra, K. J. Franz, J. B. Khurgin, Y. Dikmelik, X. Wang, J.-Y. Fan, and C. F. Gmachl, "Highly power-efficient quantum cascade lasers," *Nat. Photonics*, vol. 4, pp. 95–98, 2010.

[46] J. B. Khurgin, "Inhomogeneous origin of the interface roughness broadening of intersubband transitions," *Appl. Phys. Lett.*, vol. 93, no. 9, 091104, 2008.

[47] W. Ted Masselink, "Ionized-impurity scattering of quasi-two-dimensional quantum-confined carriers," *Phys. Rev. Lett.*, vol. 66, no. 11, pp. 1513–1516, 1991.

[48] J. V. D. Veliadis and J. B. Khurgin, "Engineering of the nonradiative transition rates in nonpolar modulation-doped multiple quantum wells," *J. Opt. Soc. Am. B.*, vol. 14, no. 5, pp. 1043–1047, 1997.

[49] J. V. D. Veliadis, J. B. Khurgin, and Y. J. Ding, "Engineering of the nonradiative transition rates in modulation-doped multiple-quantum wells," *IEEE J. Quantum Electron.*, vol. 32, no. 7, pp. 1155–1160, 1996.

[50] M. O. Manasreh, *Semiconductor Heterojunctions and Nanostructures*. New York: McGraw-Hill, 2005.